Inverted metamorphism in the High Himalaya of Himachal (NW India) : phase equilibria versus thermobarometry

Autor(en): **Vannay, Jean-Claude / Grasemann, Bernhard**

Objekttyp: **Article**

Zeitschrift: **Schweizerische mineralogische und petrographische Mitteilungen = Bulletin suisse de minéralogie et pétrographie**

Band (Jahr): **78 (1998)**

Heft 1

PDF erstellt am: **21.07.2024**

Persistenter Link: https://doi.org/10.5169/seals-59277

SCHWEIZ. MINERAL. PETROGR. MITT. 78, 107–132, 1998

Inverted metamorphism in the High Himalaya of Himachal Pradesh (NW India): phase equilibria versus thermobarometry

by *Jean-Claude Vannay*[1] and *Bernhard Grasemann*[2]

Abstract

The crystalline core of the Himalayan orogen in the Sutlej valley corresponds to a 9-km-thick, high-grade metamorphic sequence. This High Himalayan Crystalline (HHC) shows an inverted metamorphic zonation characterized, from the base to the top of the unit, by a gradual superposition of staurolite, kyanite, sillimanite, and migmatite Barrovian mineral zones. Phase equilibria constraints based on discontinuous reactions, as well as rim thermobarometry and P-T path results, indicate peak metamorphic conditions evolving from T ≈ 580 °C and P ≈ 750 MPa at the base of the HHC, to T ≈ 750 °C and P ≈ 800 MPa at the top. These data suggest that the inverted metamorphic field gradient in the HHC is probably the consequence of diachronic equilibration at different temperatures but more or less constant pressure throughout the sequence. Rim thermobarometry determinations show, however, that final equilibration throughout the HHC occurred at an almost constant temperature around T ≈ 570 °C. Comparable temperature profiles around T ≈ 600 °C in other Himalayan sections have been interpreted as the result of a thermal buffering caused by anatexis, whereas isothermal pressure variations have been invoked to explain the inverted metamorphic zonation observed in such sequences. In contrast, garnet zoning and P-T path data from the Sutlej section indicate that the apparent lack of thermal field gradient across the HHC is the consequence of retrograde re-equilibration of high-grade mineral assemblages during exhumation and cooling.

Keywords: thermobarometry, P-T path, inverted metamorphism, re-equilibration, Himalaya, Himachal Pradesh.

Introduction

One of the most enigmatic and debated feature of the Himalayan geology is the inverted metamorphic field gradient observed in the crystalline core of this orogen. This inverted metamorphic zonation, already observed by MALLET (1875), has been described in numerous sections along the entire Himalayan range. More recently, advances in thermobarometry methods allowed to place quantitative constraints on the pressure and temperature conditions during the Himalayan metamorphic evolution (e.g. HODGES and SILVERBERG, 1988; HODGES et al., 1988, 1993; HUBBARD, 1989; PÊCHER, 1989; INGER and HARRIS, 1992; SWAPP and HOLLISTER, 1991; MACFARLANE, 1995; VANNAY and HODGES, 1996). Based partly on such quantitative data, several models have been developed to explain the Himalayan inverted metamorphism. Some interpretations suggest a tectonic inversion of isograds through recumbent folding, thrusting, or shearing (e.g. BRUNEL and KIENAST, 1986; SWAPP and HOLLISTER, 1991; JAIN and MANICKAVASAGAM, 1993; and references therein). Other models invoke more complex interactions between the tectonic evolution and thermal processes such as crustal radiogenic heating, heat advection, shear heating, heat transfer between hot hanging wall and colder foot wall during thrusting, and heat focussing beneath the sediments capping the metamorphic core (e.g. HUBBARD, 1989; JAMIESON et al., 1996; DAVIDSON et al., 1997; and references therein). The variety of the proposed models, and the lack of consensus about them, is not surprising given the significant geological variations observed along-strike in the Hi-

[1] Institut de Minéralogie et Pétrographie, Université de Lausanne, CH-1015 Lausanne, Switzerland. <Jean-Claude.Vannay@imp.unil.ch>
[2] Institut für Geologie, Universität Wien, Althanstrasse 14, A-1090 Wien, Austria. <Bernhard.Grasemann@univie.ac.at>

malayan orogen, as well as the more or less complex polyphase tectonometamorphic evolution observed in some sections. The Himalayan inverted metamorphism is thus likely to remain a controversial issue until a sufficient amount of data will allow to distinguish the influence of first order processes relative to more local factors. More specifically, the limited amount of well-constrained P-T path data implies that much uncertainty remains about the meaning of rim thermobarometry results in the context of a rather complex metamorphic evolution. For instance, because of the continuous deformation associated with the exhumation and a probable diachronic equilibration at different structural levels, the temperatures determined throughout a metamorphic sequence cannot reflect neither a transient nor a steady state geotherm. Additionally, re-equilibrations subsequent to peak of metamorphism may also blur the relation between thermobarometry results and the metamorphic evolution.

The aim of the present work is to provide an additional insight into the Himalayan inverted metamorphism, from the study of a little known section through the High Himalaya of Himachal Pradesh, in NW India. Geological mapping and petrographic analyses reveal that an inverted metamorphic zonation, characterized by a gradual superposition of staurolite zone to kyanite + sillimanite bearing migmatite zone, is preserved in the high-grade metapelites of the High Himalayan Crystalline, which represents the crystalline core of the Himalayan orogen. Yet, thermobarometry, garnet zoning, and P-T path data show that rim P-T determinations throughout this sequence do not systematically record peak of metamorphism conditions, and that P-T estimates for the higher grade zones represent final equilibration at some stage of the retrograde evolution. These results suggest that re-equilibration of mineral assemblages subsequent to peak of metamorphism is a process that should be taken into account before interpreting or modelling the tectonothermal evolution of the Himalayan crystalline core in particular, or of high-grade metamorphic sequences in general.

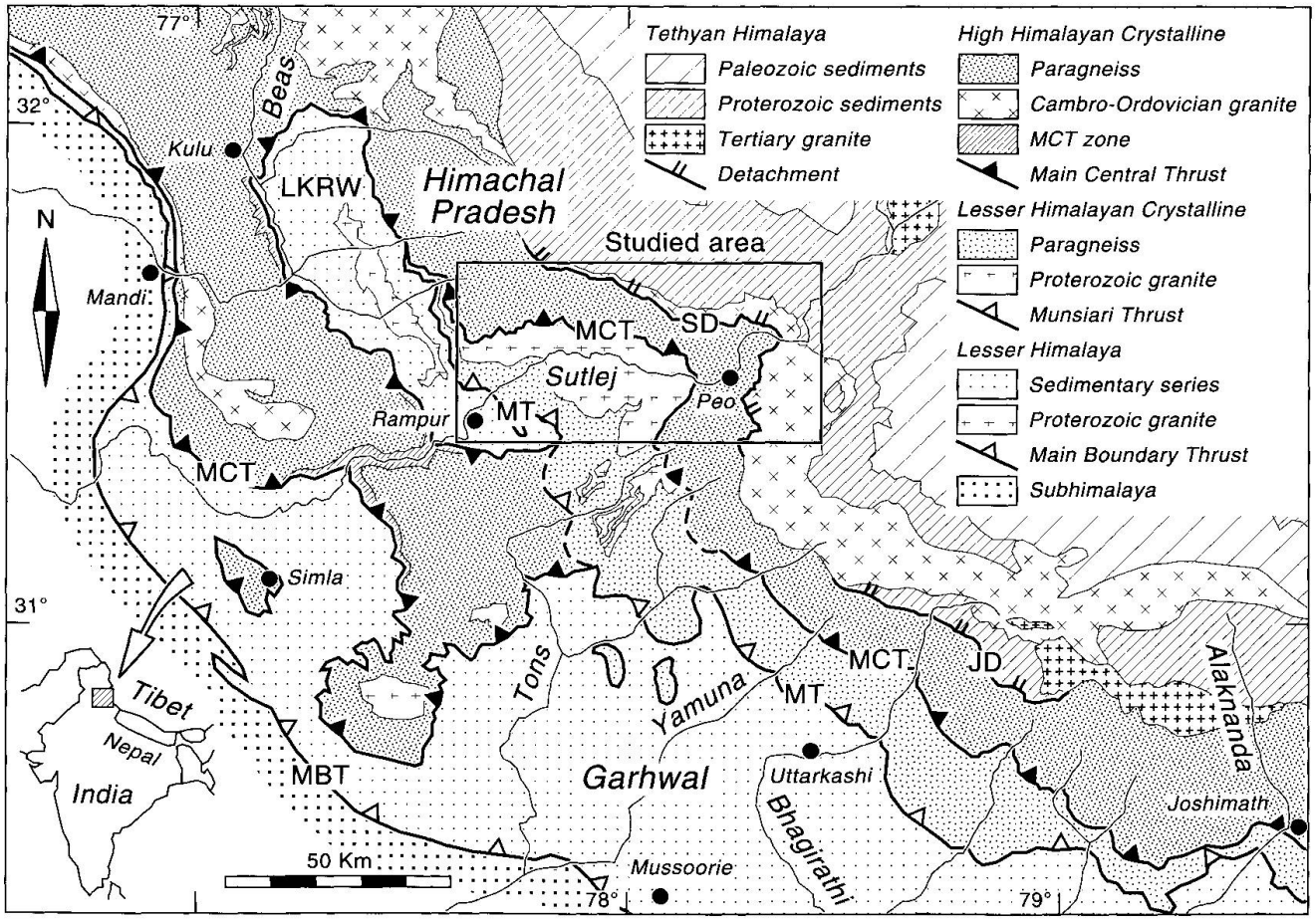

Fig. 1 Geological and geographical context of the studied area in the NW Himalaya of India. Geology compiled after TEWARI et al., 1978; VALDIYA, 1981; JAIN and ANAND, 1988; PÊCHER and SCAILLET, 1989; METCALFE, 1993; FRANK et al., 1995; and our own data. Abbreviations: MBT = Main Boundary Thrust, MT = Munsiari Thrust, MCT = Main Central Thrust, LKRW = Larji-Kulu-Rampur Window, SD = Sangla detachment, JD = Jalha detachment.

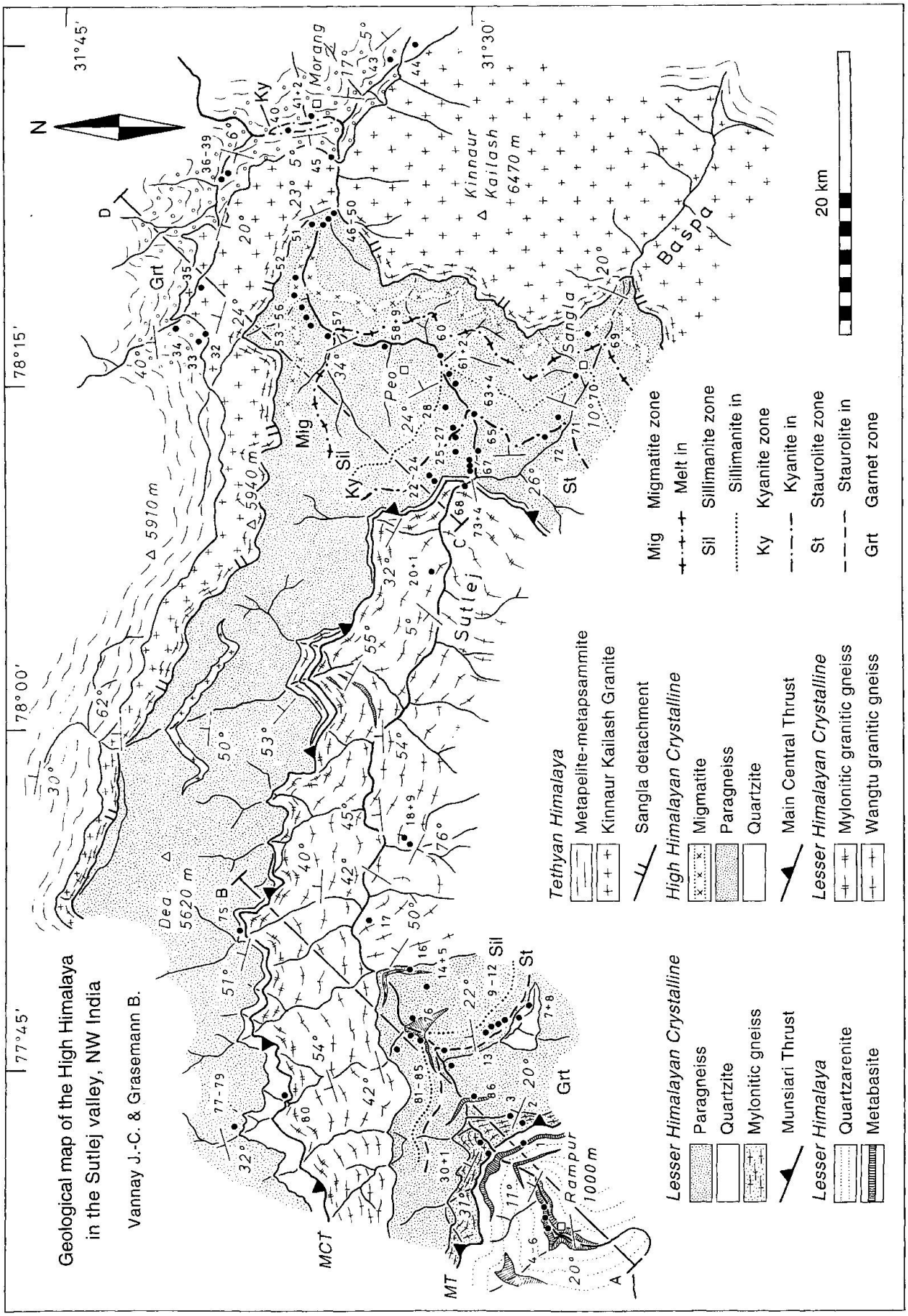

Fig. 2 Geological map of the High Himalaya in the Sutlej valley. See text for detailed description of metamorphic mineral zones in metapelitic sequences. Labelled black dots correspond to sampling locations. White dots in the Tethyan Himalaya indicate the garnet zone. Based on an original survey by the authors.

Geological setting

The Sutlej is one of the rare rivers cross-cutting entirely the High Himalayan range in its northwestern part. Along this natural cross-section, the medium to high-grade metamorphic rocks forming the core of the Himalayan orogen are exposed for a structural thickness of 25 km. Because access to this region was restricted until recently, only a few studies on the tectonic and metamorphic evolution of this area have been undertaken (e.g. BERTHELSEN, 1951; SHARMA, 1977; TEWARI et al., 1978; KAKAR, 1988; MISRA, 1993; SINGH and JAIN, 1993; GURURAJAN, 1994). Four major tectonic units are exposed along the studied part of the Sutlej traverse and these units can be correlated with what is observed in the adjacent regions of Himachal Pradesh and Garhwal (Fig. 1).

LITHOTECTONIC UNITS

Lesser Himalaya (LH)

The LH is composed of low-grade, mainly detrital sediments which represent the Upper Proterozoic to Lower Cenozoic sedimentary cover of the Indian plate (e.g. FRANK et al., 1977, 1995). This unit thrusts on the Paleogene to Neogene molasses of the Subhimalaya foreland basin along the Main Boundary Thrust (MBT). In the studied area, only the older, Precambrian sediments of the LH are exposed in a dome structure forming the southeastern part of the Larji-Kulu-Rampur Window (Figs 1 to 3). This series predominantly consists of massive beds of white quartzarenite, alternating with thinner layers of chlorite schist and quartz schist. Coarser microconglomeratic levels are observed in places. Cross bedding structures in the quartzites indicate a normal polarity for the sequence. Metavolcanics and intrusive diabases cropping out within the quartzites near Rampur gave a Sm/Nd age of 2510 ± 90 Ma (BHAT and LEFORT, 1992). To the NW of the studied area, peraluminous S-type granites and acid volcanics occur as high-level intrusives and intercalations in the quartzites, and they yielded a 1840 ± 70 Ma Rb/Sr age (FRANK et al., 1977).

Lesser Himalayan Crystalline (LHC)

The LHC corresponds to a medium to high-grade metamorphic sequence. Along the Sutlej section, the lower part of the LHC is a 8 to 9 km thick metasedimentary sequence, composed mainly of paragneiss and mica schist, with minor concordant sheets of metabasite, quartzite, and granitic gneiss. The upper part of the LHC is a 6 to 7 km thick sheet of massive granitic augen-gneiss called the Wangtu Gneiss. Geochronological Rb/Sr measurements indicate an Early Proterozoic protolith for this orthogneiss (2025 ± 86 Ma, KWATRA et al., 1986). Quartz schist and mica schist, as well as concordant sheets of metabasite, are occasionally observed in this sequence. Although the LHC shows lithological affinities with the LH, notably the presence of Early Proterozoic granitic rocks, it is a clearly distinct tectonometamorphic unit. The LHC is most probably connected to the Munsiari Group of Garhwal (VALDIYA, 1981; PÊCHER and SCAILLET, 1989; METCALFE, 1993), which is in turn probably linked to the Lesser Himalayan Crystalline of Nepal, further to the SE (PÊCHER, 1989).

High Himalayan Crystalline (HHC)

The HHC represents the crystalline core of the Himalayan orogen along the entire range. Along the Sutlej section, this 9 km thick unit is formed essentially of high-grade paragneiss, mica schist, and migmatite, with minor metabasite, calc-silicate gneiss, and granitic gneiss. A sedimentary bedding is occasionally preserved in the metapelites and, except for the higher metamorphic grade, these rocks are comparable with the basal metasediments of the overlying Tethyan Himalaya unit; they most probably represent the protolith of the HHC metamorphics. The base of the HHC is generally underlined by a 20 to 800 m thick level of white quartzite, comparable to the Precambrian sediments of the LH unit.

Tethyan Himalaya (TH)

The TH corresponds to a sequence of Upper Precambrian to Eocene sediments deposited on the margin of the Indian plate. These sediments generally underwent a very low to low-grade metamorphism. The lower part of the TH sedimentary series exposed along the Sutlej section consists mainly of metapelite and metapsammite derived from a thick and homogeneous sequence of Upper Precambrian to Lower Cambrian siltstone and sandstone. The Kinnaur Kailash Granite (KKG) intruded these metasediments. Numerous xenoliths of metasediment within the granite, as well as granitic dikes intruding the metasediments, are observed along the contact. Although no geochronological dating is available, the KKG is generally considered as belonging to a well-doc-

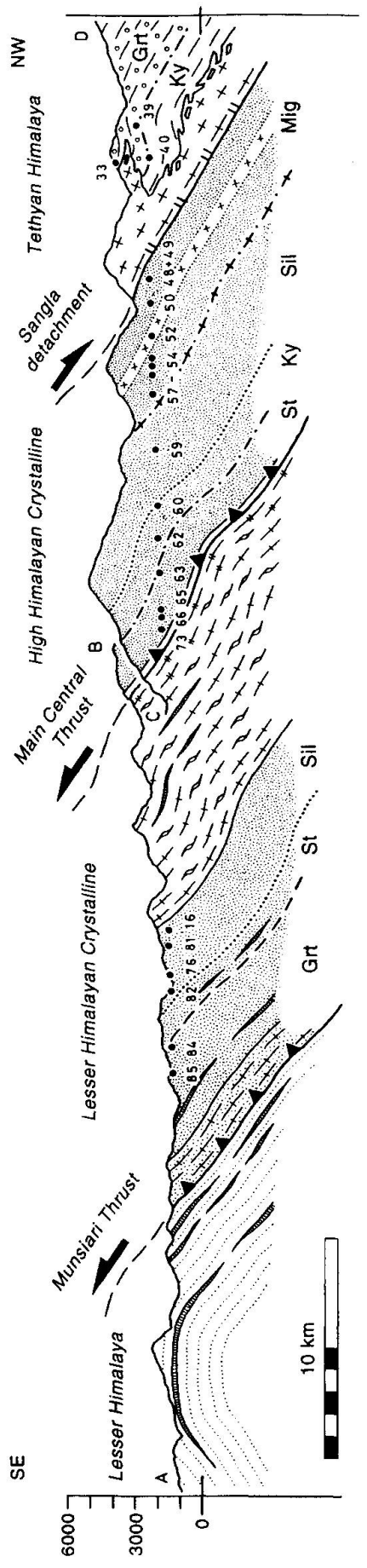

Fig. 3 Geological cross-sections for the High Himalaya in the Sutlej valley. See figure 2 for locations and symbols. The structural position of the samples analyzed for thermobarometry is indicated. Elevation in meters.

umented group of Himalayan Cambro-Ordovician granites (MISRA, 1993).

TECTONICS

Three major structures controlled the tectonometamorphic evolution of the studied units (Figs 2 and 3). The Munsiari Thrust (MT) separates the LH from the LHC. In the lowermost LHC, a 1 to 2 km thick mylonitic shear zone, composed mainly of granitic gneiss with minor paragneiss, testifies of the intense deformation associated with this thrust. Shear sense indicators associated with a penetrative stretching lineation (C-S fabrics, rotated garnets, mantled porphyroclasts) consistently indicate shearing toward the SSW. The transition between these mylonites and the overlying gneisses is gradual. A penetrative schistosity and stretching lineation in the LHC paragneiss and orthogneiss testify of ductile deformation throughout this unit. Sigmoidal inclusion trails in synkinematic poikiloblasts from the paragneiss, as well as K-feldspar mantled porphyroclasts in the orthogneiss, indicate that this deformation is associated with a significant SW-directed shearing. The second major structure is the Main Central Thrust (MCT), which marks the limit between the LHC and HHC. On both sides of this thrust, the rocks are mylonitic for some hundred of meters. Shear sense indicators in both foot wall orthogneiss (mantled porphyroclasts, shear zone) and hanging wall paragneiss (C-S fabrics, rotated garnets, shear bands, back-rotated boudins) indicate SW-directed, non-coaxial general shearing. In the LHC, relict fabrics most probably associated with the initial underthrusting of this unit below the MCT are superposed by structures related to thrusting along the MT. Geochronological data indicate that the MCT was mainly active during Early Miocene (e.g. FRANK et al., 1977; HUBBARD and HARRISON, 1989). $^{40}Ar/^{39}Ar$ geochronology results from Garhwal (METCALFE, 1993), as well as our preliminary results for the Sutlej section, show that the cooling ages become gradually younger from the top of the HHC to the base of the LHC. This trend confirms that the MT is younger than the MCT.

The third major structure is the Sangla detachment (SD), separating the HHC and TH units. Mylonitic shear zones in the lowermost part of the KKG manifest the ductile, extensional deformation related to this structure. Going upward from this contact, the mylonitic foliation fades and the granite shows little penetrative deformation in its upper part. Together with the Jhala detachment in Garhwal (Fig. 1; PÊCHER and SCAILLET, 1989;

METCALFE, 1993), the SD is most probably part of a system of Early Miocene extensional structures that acted contemporaneously with thrusting along the MCT, and which are observed at the top of the HHC in several sections along the range (e.g. HERREN, 1987; HODGES et al., 1992; DÈZES et al., submitted). Extensional structures along the SD are superposed on mylonitic compressional fabrics related to a SW-directed shearing. The SD thus probably represents the reactivation of a former thrust; such a mechanism has been already proposed by PATEL et al. (1993) and VANNAY and HODGES (1996) for comparable structures in Zanskar and Nepal. Although the main ductile extension is concentrated along the SD, more brittle extensional structures are also observed in a broad zone from the HHC to the TH units, suggesting protracted extension during the exhumation of the metamorphic sequence. Interference patterns of folds and schistosities indicate that at least two major tectonic phases are responsible for the penetrative ductile deformation observed throughout the HHC. We interpret this polyphase evolution as reflecting the initial underthrusting of the HHC below the SD, followed by its exhumation through combined thrusting along the MCT and extension along the SD.

Metamorphic petrography

The mineralogical and textural characteristics of the Sutlej section rocks have been analysed in 90 samples, mainly metapelites. In the following descriptions, the relevant mineral assemblages allowing to constrain the metamorphic peak conditions are given first, whereas the remaining minerals are within brackets. A summary of the mineral assemblages observed is given in the appendix (Tab. A1). Mineral abbreviations after KRETZ (1983) and SPEAR (1993).

METAPELITES

Mineral assemblages in metapelitic rocks allow to distinguish five Barrovian metamorphic mineral zones. The distribution of these zones in the studied section indicates that both LHC and HHC units preserved inverted metamorphic field gradients. From base to top, a gradual succession of garnet, staurolite, and sillimanite zones is observed in the LHC, whereas the HHC shows a superposition of staurolite, kyanite, sillimanite, and migmatite zones (Figs 2 and 3). The TH shows a superposition of garnet on kyanite zone assemblages, characteristic of a normal metamorphic zonation. To the N of the studied section, the metamorphic grade in the TH further decreases up section to biotite zone and chlorite zone conditions (SHARMA, 1977).

The mineral assemblages typical for each metamorphic zone show only slight variations from one unit to another. Our interpretation of the pressure and temperature stability conditions of the characteristic assemblages in metapelites is based on a composite petrogenetic grid adapted to the observed compositions (Fig. 5). Most of the reactions limiting these stability fields have a steep dP/dT slope, implying a strong temperature control on the characteristic mineral equilibria.

Garnet zone

In the LHC and TH units, the garnet zone rocks generally contain the stable assemblage Grt + Bt + Chl + Ms + Qtz + Pl (± Ep ± Cal). The micas and the chlorite define the main schistosity in these rocks. Frequent sigmoidal inclusion trails in garnet indicate a synkinematic growth of this phase during a SSW to SW-directed shearing. In the lowermost LHC unit, one sample contains abundant margarite in stable assemblage with Grt + Bt + Chl + Ms + Qtz ± Pl (+ Ep) (Fig. 4a). Some margarite in two structurally higher samples probably represent a relict prograde phase. The stability of Grt + Bt + Chl + Ms + Qtz + H_2O is limited by the reactions (1) and (3) in the MnKFMASH system (for X_{sps} up to 0.2, the maximum content in the analysed garnets), constraining the temperature between T ≈ 460 and 610 °C (Fig. 5). The association of Grt + Bt + Chl + Mrg + Qtz + H_2O in the lowermost LHC is limited by reactions (1), (7), and (8) in the CKNASH system, indicating T ≈ 460–580 °C and P ≤ 1000 MPa.

Staurolite zone

In both the LHC and HHC units, the assemblage characteristic of the staurolite zone is St ± Grt + Bt ± Chl + Ms + Qtz + Pl (+ Ep), although the assemblage Grt + Bt ± Chl + Ms + Qtz + Pl is also common, most likely because of variations in bulk rock composition. The penetrative schistosity is defined by Bt + Ms ± Chl ± St. The staurolite is synkinematic and it appears either as euhedral, prismatic crystals oriented parallel to the schistosity, or as poikilitic blasts containing slightly sigmoidal inclusion trails (Fig. 4b). The garnet shows sigmoidal inclusion trails marked by Bt + Ms ± Qtz ± Pl ± Chl ± oxides. Rare post-kinematic chlorite grew as randomly oriented flakes superposed

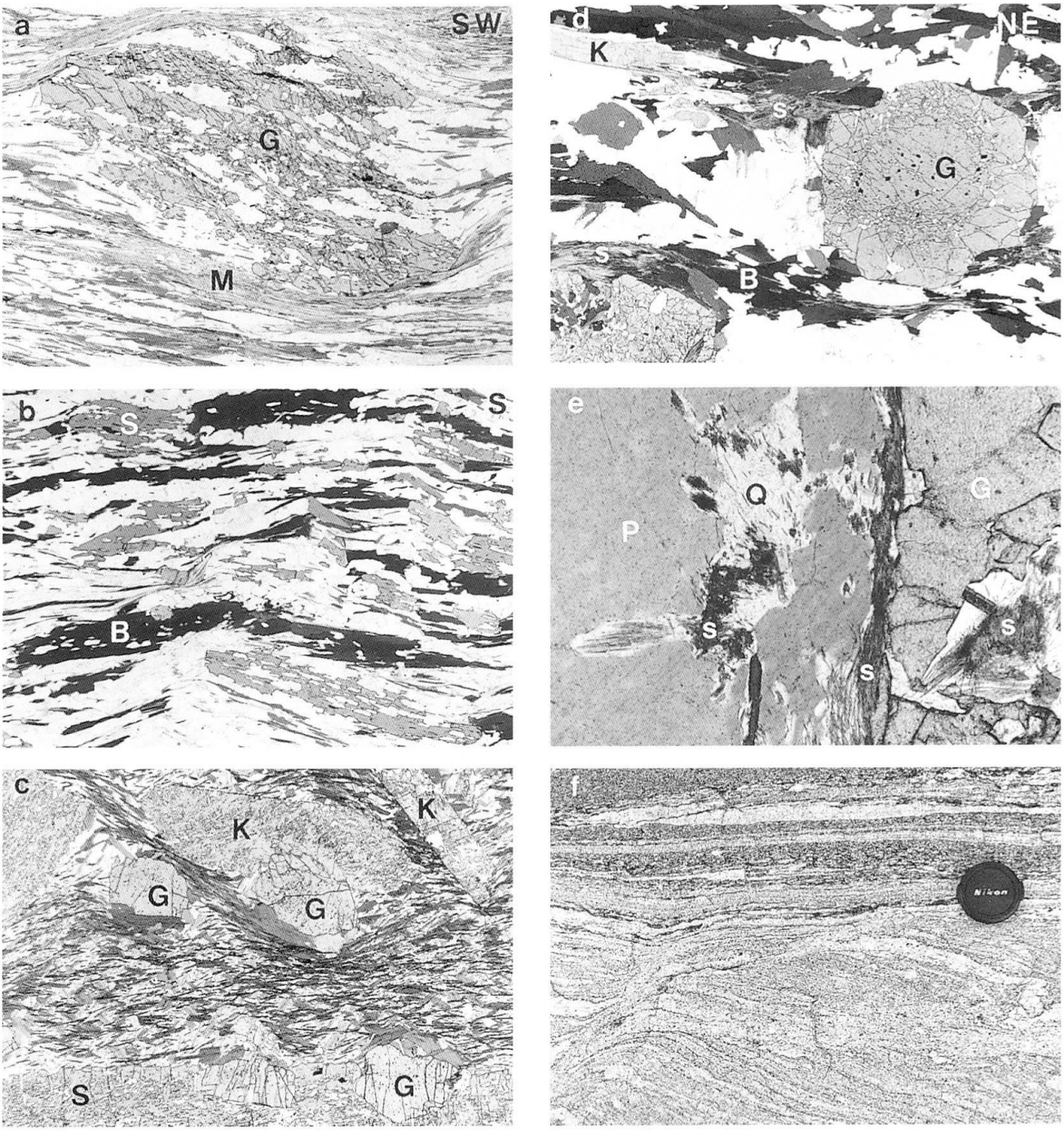

Fig. 4 Selected petrographic observations. The scale given within brackets, together with sample number and unit, corresponds to the long dimension of the image, whereas the orientation is indicated in the upper right corner. (a) Synkinematic garnet (G) in a margarite-bearing (M) paragneiss from the garnet zone [6 mm, sample 31, LHC]. (b) Synkinematic staurolite (S) in a biotite-bearing (B) paragneiss from the staurolite zone [8 mm, sample 12, LHC]. (c) Poikiloblastic kyanite (K) and staurolite overgrowing garnet in a kyanite zone paragneiss [10 mm, sample 40, TH]. (d) Sillimanite (s) and kyanite bearing paragneiss from the migmatite zone [12 mm, sample 55, HHC]. (e) Detail of sample 55. Fine-grained, fibrolitic sillimanite growing with quartz (Q) at the expense of plagioclase (P) along a plagioclase-garnet interface. Sillimanite associated with biotite also occurs as inclusions within garnet [1.5 mm]. (f) Migmatitic paragneiss from the upper HHC. The dark parts correspond to sillimanite and kyanite bearing paragneiss, whereas the clear parts represent granitic segregations [50 cm].

on the schistosity. The stability of St ± Grt + Bt ± Chl + Ms + Qtz + H_2O is limited by the reactions (2) and (4) in the KFMASH system (Fig. 5), suggesting a temperature range of T ≈ 560–620 °C for a Barrovian-type metamorphism.

Kyanite zone

This zone is characterized by the assemblage Ky ± St + Grt + Bt ± Chl + Ms + Qtz + Pl (± Ep ± Rt ± Ilm). In the HHC, the kyanite appears as euhedral prisms oriented parallel to the penetrative schistosity. In the lower part of the TH, the kyanite zone crops out as a restricted metamorphic window exposed by the Sutlej river near Morang (Fig. 2). In these rocks, kyanite and staurolite form large (up to 5 cm), euhedral poikiloblasts generally overgrowing the garnet (Fig. 4c). The garnet frequently shows sigmoidal inclusion trails proving a synkinematic growth with respect to the penetrative schistosity marked by the micas. Chlorite appears only as a rare, post-kinematic, retrograde phase. The stability of Ky + St + Bt + Ms + Qtz + Pl + H_2O is limited in the petrogenetic grid by the reactions (4), (6), and (9), as well as by the Ky = Sil equilibria, indicating a P-T range of T ≈ 610–720 °C and P ≈ 600–1100 MPa. Because the kyanite zone assemblage in the HHC does not contain staurolite, its stability could be extended to higher P-T conditions. Yet, the superposition along a continuous field gradient of stable sillimanite + kyanite bearing assemblages on the kyanite zone rocks rather suggests that such conditions have not been reached.

Sillimanite zone

The assemblage characteristic of this zone is Sil + Ky ± St + Grt + Bt + Ms + Qtz + Pl (± Ep ± Rt). Sillimanite and kyanite are present in numerous samples (Tab. A1) and both aluminosilicates generally appear to be stable. Kyanite forms euhedral prisms up to 1 cm long, whereas sillimanite occurs as fine-grained fibrolite closely associated with biotite and/or plagioclase. The penetrative schistosity in these rocks is generally defined by Bt + Ms ± Sil ± Ky. In the LHC rocks, staurolite is common and generally forms either euhedral prisms oriented parallel to the schistosity, or poikilitic blasts containing linear or slightly sigmoidal inclusion trails. The sillimanite zone rocks of the HHC do not contain staurolite, suggesting either higher metamorphic conditions, or Mg-richer bulk rock composition compared to the LHC metapelites. Synkinematic garnet appears either as euhedral grains containing sigmoidal inclusion trails, or as elongated, skeletal poikiloblasts parallel to the schistosity. Chlorite is not part of the peak assemblage, but it occurs in the LHC rocks as a relict prograde phase included, together with biotite, muscovite, and quartz, within garnet and staurolite. The peak assemblage typical of the sillimanite zone indicates conditions close to the Ky = Sil equilibria, above the reaction (4), and most probably above reaction (5) given the complete absence of synkinematic chlorite. The stability of Ms + Pl, as well as the lack of widespread anatectic melt, implies a temperature below the vapor absent melting reaction (11) for Ms + Pl + Qtz bearing paragenesis. P-T conditions are thus constrained as T ≈ 610–720 °C and P ≈ 600–850 MPa (Fig. 5).

Migmatite zone

The metapelites from the upper part of the HHC are migmatitic and granitic segregations become widespread in the uppermost levels of this sequence. The characteristic assemblage in this zone is Melt + Sil + Ky + Grt + Bt ± Ms + Qtz + Pl ± Kfs. Except for the partial melting, the mineralogical and textural characteristics of these metapelites are comparable to those of the underlying sillimanite zone rocks. Euhedral kyanite and fibrolitic sillimanite are stable synkinematic phases marking the schistosity together with biotite and muscovite (Fig. 4d). Most samples contain both aluminosilicates, muscovite, and scarce K-feldspar, indicating high alumina compositions in the CKNASH system. In some aluminosilicate-free samples containing K-feldspar, muscovite is rare or absent suggesting more potassic bulk compositions. Anatectic segregations in the metapelites contain the assemblage Kfs + Pl + Qtz + Bt + Ms ± Grt (Fig. 4f).

The stable coexistence of kyanite and sillimanite implies metamorphic peak conditions close to the Ky = Sil equilibria. Partial melting of water-saturated Ms + Pl + Qtz bearing metapelitic assemblages can begin at a temperature as low as T ≈ 650 °C (Fig. 5, reaction 10). Such vapor present melting would, however, produce only a limited amount of melt as the reaction consumes the available volatile phase and is shifted to higher temperatures (Spear, 1993). Additionally, it is not likely that the considered rocks had a significant porosity at the crustal depths implied by their mineral assemblages. It is therefore more likely that the widespread in-situ anatexis is the consequence of a vapor absent melting reaction (Harris et al., 1993). The minimal conditions for vapor absent melting of Ms + Pl + Qtz bearing

metapelites correspond to the reaction (11) in figure 5. The presence of muscovite and plagioclase in these metapelites restricts the maximal metamorphic conditions below the upper stability limit for this sub-assemblage (Fig. 5, reaction 12). Consequently, we estimate that the peak conditions reached in the migmatite zone are T ≈ 700–780 °C and P ≈ 750–950 MPa.

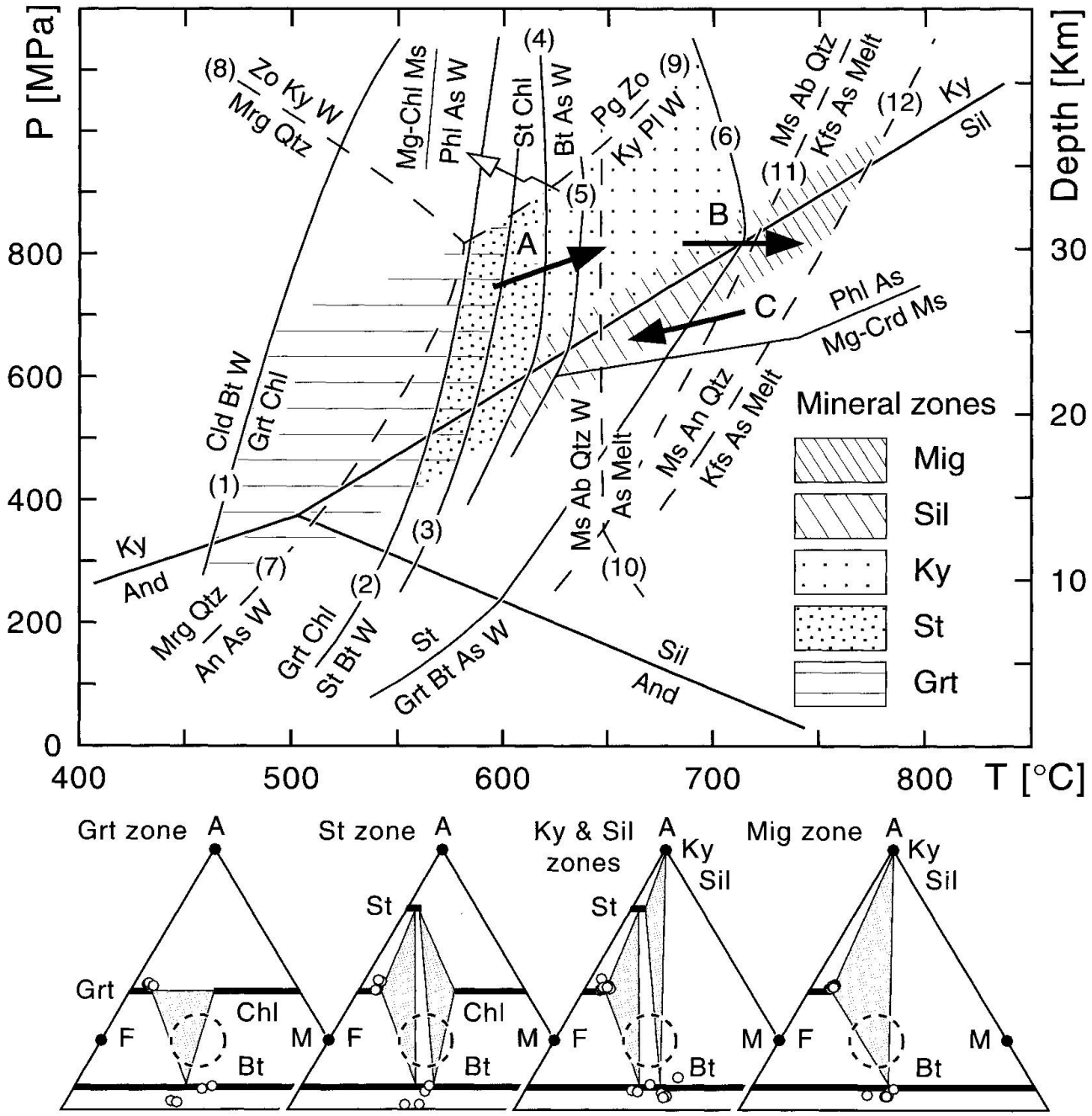

Fig. 5 Composite petrogenetic grid for the metapelites in the Sutlej section. The P-T stability fields for the mineral assemblages characteristic of the observed mineral zones are presented. Solid and dashed lines correspond to reactions in the (Mn)KFMASH and CKNASH systems, respectively. Because the range of X_{sps} in the analysed garnets varies between ~ 2 to 20%, the MnKFMASH reactions (1) and (3) that limit the garnet zone field are plotted for X_{sps} = 0.2. The reaction (2) is the KFMASH equivalent of reaction (3). The legend for reaction (5) is indicated by the white arrow. Reactions (1) to (9) after SPEAR (1993). The vapor present melting reaction (10) represents the minimum conditions for anatexis in water-saturated (X_{H_2O} = 1) Ms + Pl + Qtz bearing metapelites, whereas the reactions (11) and (12) correspond to vapor absent melting conditions (THOMPSON and TRACY, 1979; LEBRETON and THOMPSON, 1988). The arrows indicate P-T path segments inferred from the textural relations discussed in text. The mineral assemblages characteristic of the various zones are summarized in AFM diagrams, together with the composition of garnet and biotite (small dots), and the composition range of low-Al pelites (dashed circles).

METABASITES

Metabasites cropping out as concordant sheets within the massive quartzites of the LH contain the assemblage Act + Ab + Ep + Chl (+ Bt + Qtz ± Cal ± Rt) typical of the greenschist facies. This assemblage broadly constrains the metamorphic conditions as T ≈ 280–500 °C (SPEAR, 1993). In the garnet zone of the LHC unit, metabasites contain the stable assemblage Hbl + Pl (ab–olg) + Ep + Chl (+ Bt + Qtz ± Cal ± Rt), characteristic of the epidote amphibolite facies. The P-T conditions indicated by this assemblage (T ≈ 500–650 °C and P ≈ 300–1100 MPa) are compatible with those implied by the paragenesis in metapelites. The transition from garnet zone to staurolite zone conditions in the LHC metapelites occurs in parallel with the disappearance of epidote and chlorite in metabasites. The stable assemblage in the mafic rocks becomes Hbl + Pl (olg-and) (+ Bt + Qtz ± Ttn), marking the passage to the amphibolite facies. The temperature range for the stability of this assemblage is broadly T ≈ 550–700 °C. Concordant metabasites in the Wangtu Gneiss contain the same paragenesis. Metabasites from the HHC kyanite and migmatite zones contain Hbl + Pl ± Grt ± Cpx (+ Bt + Qtz ± Ttn). This assemblage demonstrates amphibolite facies conditions (T ≈ 650–800 °C) compatible with those inferred for the metapelitic assemblages.

GRANITIC GNEISSES

The typical assemblage in the Wangtu Gneiss is Qtz + Pl + Kfs + Bt + Ms + Ep. The K-feldspar generally occurs as large pre-kinematic clasts. Quartz and plagioclase recrystallized in a polygonal tex-

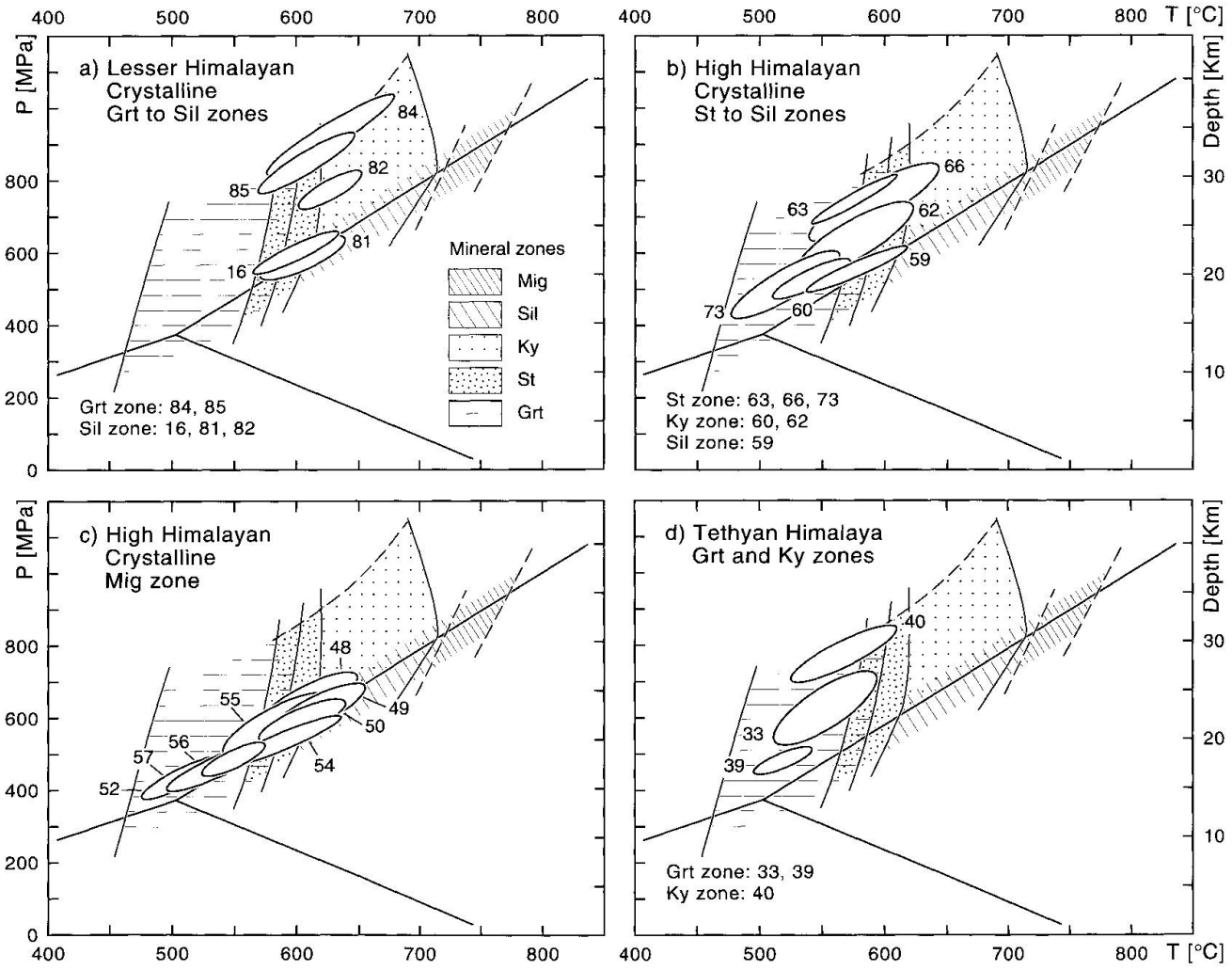

Fig. 6 Rim P-T estimates for the metapelites in the Sutlej section. Analytical and calculation procedures are presented in Appendix 1. Thermobarometers and calibrations are listed in table A2. Ellipses represent 2σ precision (95% confidence level) and their labels correspond to sample numbers (see Figs 2 and 3 for location). For clarity, only GARB-GMAP results are presented. Paleodepth based on a 27 MPa/km lithostatic gradient (average rock density: 2750 kg/m³). Mineral zone P-T stability fields as in figure 5.

Tab. 1 Summary of thermobarometry results.

Sample*	H†	Thermobarometer#	T [°C]	± 2σ	P [MPa]	± 2σ
85	3.82	GARB-GMAP	610	40	850	90
84	4.58	GARB-GMAP	630	50	930	110
82	6.11	GARB-GMAP	630	30	780	50
76	6.64	GARB	610	40	–	–
81	7.4	GARB-GMAP	610	40	590	60
81	7.4	GARB-GASP	610	40	620	70
16	8.17	GARB-GMAP	600	30	600	60
16	8.17	GARB-GASP	600	40	630	60
73	15.57	GARB-GMAP	520	40	510	90
66	15.88	GARB-GMAP	590	50	740	110
65	16.11	GARB	580	60	–	–
63	16.72	GARB-GMAP	580	40	750	70
62	17.25	GARB-GMAP	580	50	640	100
62	17.25	GARB-GASP	580	50	660	120
62	17.25	GARB-GRAIL	580	40	650	40
60	18.02	GARB-GMAP	540	30	530	50
60	18.02	GARB-GASP	540	30	540	60
59	19.85	GARB-GMAP	580	40	560	60
59	19.85	GARB-GASP	580	40	570	70
57	21.6	GARB-GMAP	540	40	480	70
57	21.6	GARB-GASP	540	40	470	70
56	22.06	GARB-GMAP	550	30	490	50
56	22.06	GARB-GASP	550	30	490	50
55	22.21	GARB-GMAP	590	40	580	90
55	22.21	GARB-GASP	590	50	600	100
54	22.37	GARB-GMAP	590	50	540	70
54	22.37	GARB-GASP	590	50	570	80
52	22.82	GARB-GMAP	510	30	440	60
50	23.43	GARB-GMAP	600	30	600	60
50	23.43	GARB-GASP	610	40	620	70
49	23.97	GARB-GMAP	620	40	630	80
49	23.97	GARB-GASP	620	40	660	80
48	23.97	GARB-GMAP	610	40	640	90
48	23.97	GARB-GASP	610	50	650	100
40	26.87	GARB-GMAP	570	40	780	80
40	26.87	GARB-GASP	570	40	780	90
39	28.02	GARB-GMAP	520	20	480	40
33	28.02	GARB-GMAP	550	40	630	100

* Mineral assemblages are summarized in table A1. †H = Orthogonal distance to Munsiari Thrust [km]. # Thermobarometer acronyms and calibrations are listed in table A2.

ture during metamorphism and they also form myrmekitic associations growing at the expense of the K-feldspar. These rocks systematically show a penetrative schistosity marked by biotite and muscovite. Retrograde chlorite is rare. The KKG generally preserved its original igneous texture and most of its magmatic assemblage, which consists of Kfs + Pl + Qtz + Bt. The metamorphic mineral phases observed are epidote, green biotite, chlorite, and rare garnet. The K-feldspar clasts show flame perthites, bent twins, and incipient recrystallization. The quartz shows abundant subgrains and incipient recrystallization. Together with the metamorphic assemblage, these microstructures broadly suggest upper greenschist to epidote amphibolite facies conditions (T ≈ 400–650 °C), and a significant metamorphic grade contrast compared to the underlying migmatitic paragneiss of the HHC.

Thermobarometry

To quantify the equilibration P-T conditions throughout the studied section, 24 metapelitic samples have been analysed for garnet biotite (GARB) thermometry, as well as for garnet-biotite-muscovite-plagioclase (GMAP) and garnet-aluminosilicate-quartz-plagioclase (GASP) barometry. The selected samples show textural characteristics suggesting equilibrium between the major phases and a minimum influence of retrograde reactions. Analytical procedure and mineral compositions are given in Appendix 1.

RIM P-T ESTIMATES

Rim P-T estimates are presented in figure 6 and summarised in table 1. These results are also plotted in figure 7 as a function of the structural position of the samples in the section. Besides textural evidences, several characteristics of the thermobarometry results suggest that the analysed mineral assemblages correspond to well-equilibrated systems. First, P-T determinations for kyanite-bearing and for kyanite + sillimanite bearing assemblages are in good agreement with the stability conditions for the aluminosilicate(s) they respectively contain. Second, P-T results obtained with two independent sets of thermobarometer (GARB-GMAP, GARB-GASP) for aluminosilicate-bearing rocks are generally similar within uncertainties (Tab. 1). An additional independent pressure estimate was obtained for one of these samples (sample 62) with the Grt-Rt-As-Ilm-Qtz (GRAIL) barometer. This equilibria is characterized by a limited sensitivity to temperature variations because of its low dP/dT slope and it yielded a pressure estimate consistent with GMAP and GASP determinations. Third, multiple equilibria calculations (BERMAN, 1991) show that the six possible reactions in each of the 13 aluminosilicate-bearing samples analysed (not presented) intersect in a restricted range of P-T conditions (average ranges: T ≈ 30 °C, P ≈ 110 MPa).

Lesser Himalayan Crystalline

P-T estimates for the LHC metapelites fit, within uncertainties, the stability conditions deduced

from the petrogenetic grid for the garnet to sillimanite zone mineral assemblages (Fig. 6a). The average temperatures all cluster around T ≈ 610 ± 10 °C, suggesting no significant thermal field gradient in the unit. In contrast, barometric determinations reveal a significant pressure decrease from the garnet zone (P ≈ 900 MPa) to the upper sillimanite zone (P ≈ 600 MPa), suggesting that equilibration at different pressures but constant temperature could be responsible for the metamorphic zonation in the LHC. The maximum pressure measured for the LHC implies a minimum burial depth of ≈ 33 km (assuming a lithostatic pressure gradient of 27 MPa/km).

High Himalayan Crystalline

The lowermost HHC sample selected for thermobarometry corresponds to a staurolite-bearing metapelite (sample 73) collected in the mylonitic zone just above the MCT. Compared to the stability conditions for staurolite zone assemblages inferred from the petrogenetic grid, this sample yielded lower P-T results (Fig. 6b) probably because of a retrograde re-equilibration triggered by deformation and/or fluid circulation along the thrust. Except for this sample, P-T estimates for the staurolite zone are in good agreement with the phase equilibria constraints and they indicate

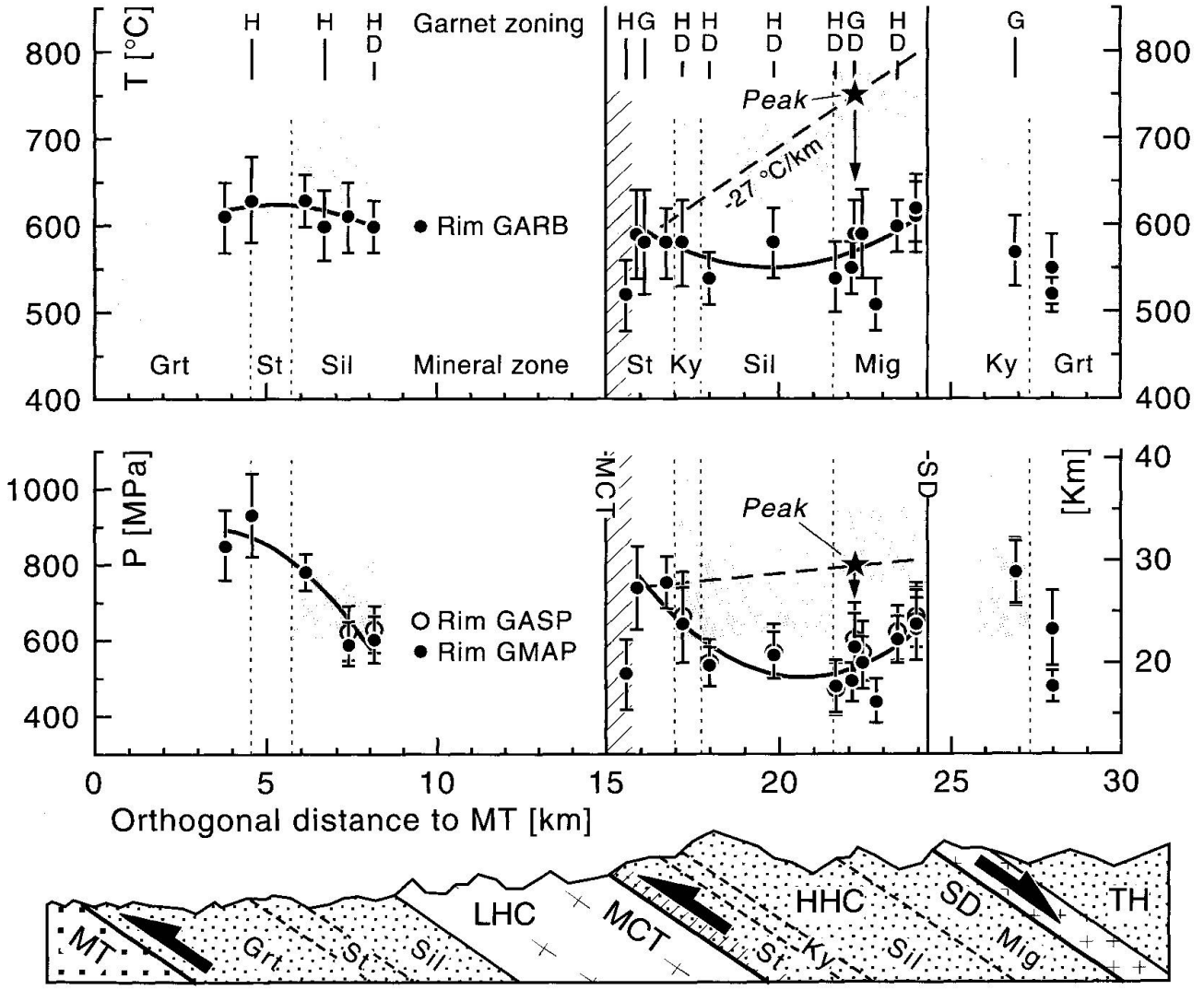

Fig. 7 Pressure and temperature profiles for the Sutlej section, based on the results presented in figure 6 and table 1. Shaded fields represent the P-T range for the stability of the various characteristic mineral assemblages, as deduced from the petrogenetic grid (Fig. 5) and discussed in text. Stars indicate peak metamorphic conditions for the HHC migmatite zone, as determined through thermodynamic modelling. Solid lines represent curve fits for the rim P-T data. Dashed lines correspond to a linear approximation of the peak metamorphic field gradient in the HHC, as discussed in text. Abbreviations for garnet zoning: H = homogeneous compositional profile, G = bell-shaped growth zoning, D = retrograde diffusional zoning at rim. The cross-section summarizes the geological setting presented in figure 3.

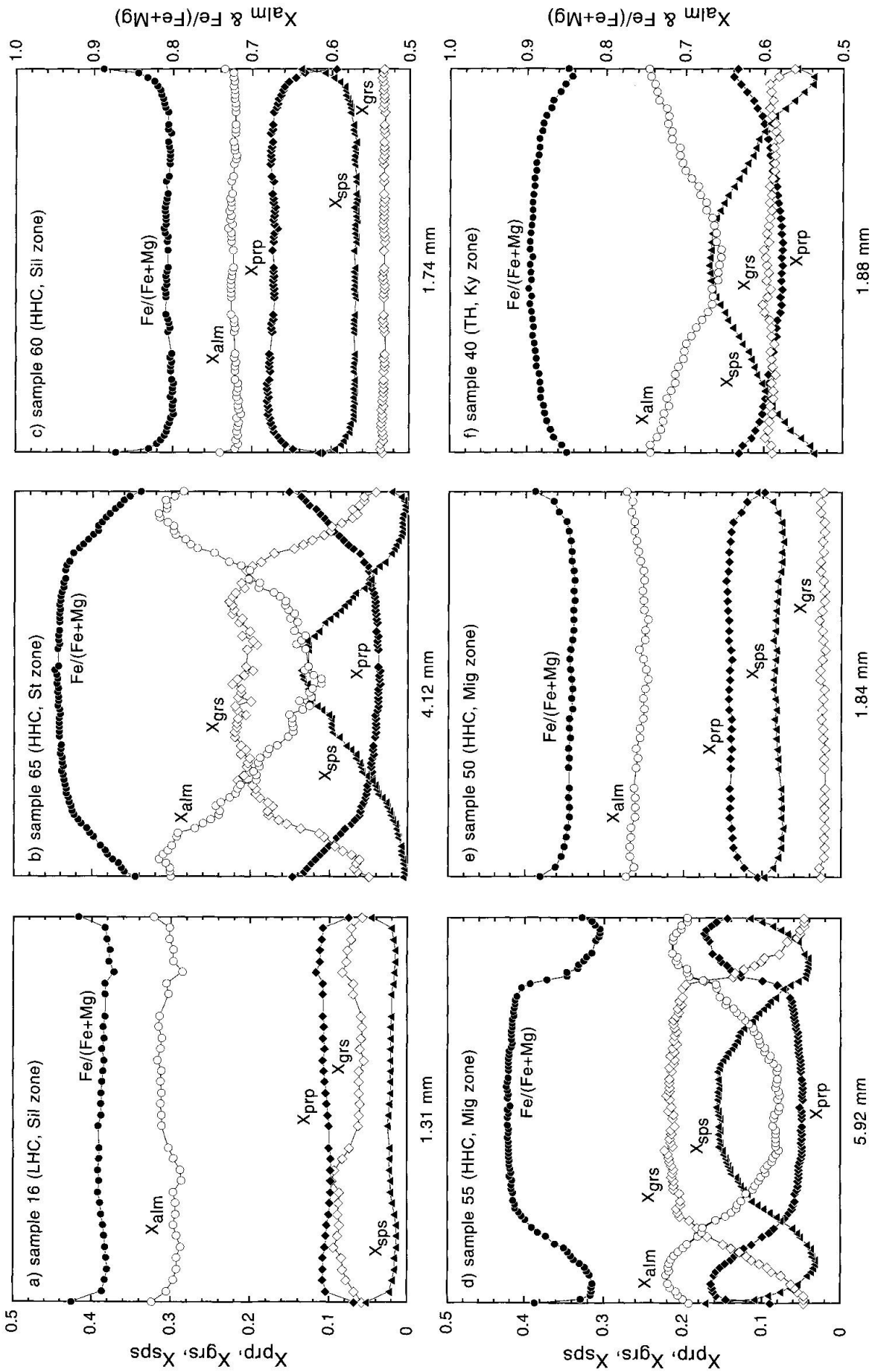

Fig. 8 Representative garnet zoning profiles from the metapelites in the Sutlej section.

peak conditions at T ≈ 580 °C and P ≈ 750 MPa (Fig. 6b). In contrast, temperature estimates for the kyanite zone appear too low with respect to the P-T conditions determined from discontinuous reactions (Fig. 6b). A comparable discrepancy is observed for a Sil + Ky bearing sample from the sillimanite zone (Fig. 6b), even if the P-T determination correctly plot on the Ky = Sil equilibria. This discrepancy is best illustrated by the results for the migmatite zone samples (Fig. 6c). Although the P-T estimates are consistent with the presence of both kyanite and sillimanite in these metapelites, the rim temperatures appear insufficient to allow the vapor absent melting inferred to account for the widespread anatexis. According to the petrogenetic grid, the measured temperatures would not even induce vapor present melting of water-saturated metapelites (Fig. 5, reaction 10). It appears consequently that, despite the inverted temperature field gradient implied by the superposition of mineral assemblages in the HHC, GARB rim thermometry indicates that the entire sequence reached final equilibration at an almost constant average temperature around 570 ± 30 °C (Fig. 7). Considering the uncertainties on temperature determinations (± 40 °C in average), no clear temperature field gradient in the HHC can be put in evidence by GARB rim thermometry. The highest rim pressure estimates in the HHC have been determined for the staurolite zone rocks (P ≈ 750 MPa). These estimates most likely represent the metamorphic peak in this zone and they indicate a minimum burial depth of ≈ 28 km. Above the staurolite zone, rim pressure estimates decrease gradually through the kyanite and sillimanite zones to reach P ≈ 500 MPa at the base of the migmatite zone. Rim pressure estimates then increase up section through the migmatite zone to reach P ≈ 650 MPa at the top of the HHC. The discrepancy between rim thermobarometry results and phase equilibria constraints for the kyanite to migmatite zones implies that these pressure estimates probably underestimate peak conditions.

Tethyan Himalaya

P-T estimates for the TH garnet zone samples are in good agreement with phase equilibria constraints and they indicate a metamorphic peak at T ≈ 530 °C and P ≈ 550 MPa. As for the HHC, the temperature measured for the TH kyanite zone appears to underestimate peak conditions.

GARNET ZONING

To characterise the zoning in garnets, a composition traverse has been measured in 12 of the samples analysed for thermobarometry. Small size garnets (≤ 2 mm) from all the metamorphic zones generally show very homogeneous compositional profiles in the core (Figs 8 a, c, and e). This zoning indicates an homogenisation of the garnet composition through diffusion at high temperature. Some larger garnets in the HHC and TH show bell-shaped compositional profiles characterized by core to rim Fe/(Fe + Mg) and X_{sps} decrease, and parallel X_{alm} and X_{prp} increase (Figs 8 b, d, and f). Such a typical growth zoning suggests a sequence of equilibrium compositions that has not been significantly re-equilibrated through diffusion at high temperature, and it is observed in rocks from the staurolite, kyanite, and migmatite zones (Fig. 7). The coexistence of bell-shaped and homogeneous garnet zoning within the same metamorphic zone (e.g. Figs 8 d and e) appears to be correlated with the garnet grain size. This feature supports the interpretation that the growth zoning in small garnets has been obliterated by diffusional re-equilibration. Throughout the HHC kyanite to migmatite zones, as well as in the uppermost LHC sillimanite zone, the garnets systematically show retrograde zoning at their outermost rim (Figs 8 a, c, d, and e). This near rim zoning is characterized by an increase in Fe/(Fe + Mg) ratio toward the rim and it indicates Fe–Mg exchange between garnet and biotite during cooling. Rocks from the LHC garnet zone and the HHC staurolite zone do not show such a diffusional zoning (Figs 7 and 8b).

P-T path

METAMORPHIC REACTIONS

No tectonic discontinuities have been observed between the various metamorphic zones within the metapelites of the LHC and HHC. The continuous change in metamorphic conditions suggests that the inverted metamorphic field gradients in these units are not the result of post-metamorphic thrusting. The absence of relictic, higher grade phases in lower grade assemblages indicates that the inverted field gradients are not the consequence of variable retrogression at different structural levels. The mineral assemblages characterizing the various zones are related to a prograde metamorphic evolution. Petrographic features allow to place some constraints on this evolution.

The close association of kyanite and staurolite generally overgrowing garnet in some kyanite-bearing rocks (Fig. 4c), as well as the removal of chlorite in these rocks, suggest that the reaction St + Chl = Bt + As + H_2O (Fig. 5, reaction 4) represents the kyanite isograd in the studied area. Together with the almost systematic presence of plagioclase in kyanite-bearing assemblages, these features imply a prograde path below the reaction (9) in the kyanite stability field (Fig. 5, arrow A). In some Sil + Ky bearing rocks from the LHC and HHC, small kyanite grains occur as relict inclusions within plagioclase blasts, probably as the result of the continuous reaction Grt + As + Qtz = Pl (= GASP barometer). These plagioclase-coated kyanites imply a prograde path less steep than the dP/dT slope of the GASP reaction in the kyanite field (≈ 1.5 MPa/°C).

In the migmatite zone metapelites of the upper HHC, some large garnets show an homogenous core containing small inclusions, a more poikilitic inner rim, and an inclusion-poor outer rim, suggesting a two-stage growth. In these rocks, sillimanite is closely associated with biotite in the matrix as well as in the outer rim of some garnets, staurolite is absent, and kyanite occurs as a stable phase in the matrix, as well as scarce inclusions in garnet (Figs 4 d and e). These features suggest a prograde path crossing the reaction St = Grt + Bt + As + H_2O (Fig. 5, reaction 6) close to the Ky = Sil equilibria (Fig. 5, arrow B).

In the same assemblages, Pl + Qtz and Pl + Ms symplectitic intergrowths developed at the expense of K-feldspar, suggesting a beginning of retrograde evolution through reaction (11). Besides the synkinematic sillimanite growing in close association with biotite in the matrix, some migmatitic metapelites contain a second generation of sillimanite developed preferentially along garnet-plagioclase contacts. This sillimanite corresponds to fine-grained fibrolite that formed, together with quartz, at the expense of plagioclase (Fig. 4e). We interpret this assemblage as the result of retrograde re-equilibration through the continuous reaction Pl = Grt + Sil + Qtz (= GASP barometer). This interpretation implies that the early stage of the retrograde path had a slope less steep than the dP/dT slope for this reaction at peak conditions (≈ 1.5 MPa/°C). Such a retrograde path (Fig. 5, arrow C) is consistent with the apparent stability of the kyanite in sillimanite-bearing rocks, as well as with the absence of typical low-pressure phases, such as cordierite or andalusite, in the studied section. Except for the garnet zone assemblages, chlorite generally appears only as a rare retrograde phase formed mainly at the expense of biotite, and more rarely of staurolite or garnet. Retrograde chlorite is generally restricted to fractures, shear zones, or to the hinge zone of late, kink-type microfolds, suggesting that deformation and fluid circulation along these structures triggered late retrograde reactions.

THERMODYNAMIC MODELLING

For a given mineral assemblage and chemical system, the conditions of equilibrium can be described by a set of differential thermodynamic equations relating the pressure, temperature, and phase compositions. Because such a system of equations has a mathematical variance equal to the thermodynamic variance of the considered assemblage, it can be solved if a corresponding number of independent variables can be determined. P-T path reconstruction through Gibbs modelling method consists in computing changes in pressure and temperature as a function of changes in the composition of phases coexisting as a series of equilibria, such as a zoned porphyroblast and its inclusions (SPEAR and SELVERSTONE, 1983; SPEAR, 1993).

One sample from the HHC migmatite zone (sample 55) appears suitable for the application of this method. This sample contains relatively large garnets which preserved growth zoning (Fig. 8d). The mineral assemblage in sample 55 is Sil + Ky + Grt + Bt + Ms + Pl + Qtz (Fig. 4d). The garnet contains inclusions of biotite, muscovite, quartz, and plagioclase, as well as sillimanite in the outer rim. In similar assemblages from the same metamor-

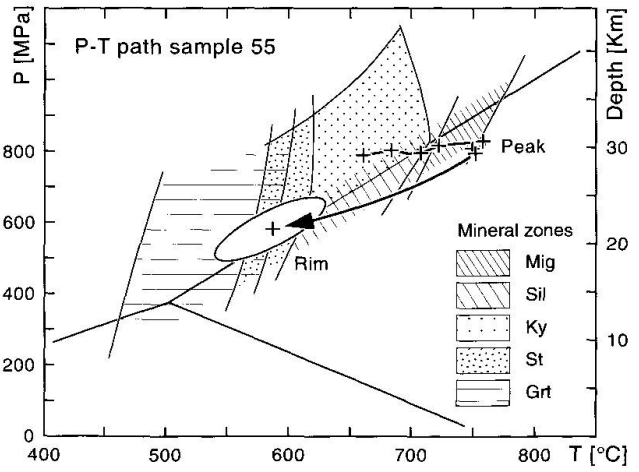

Fig. 9 P-T path for sample 55 from the upper HHC migmatite zone, calculated through Gibbs modelling method (see Figs 2 and 3 for location). Analytical procedure and modelling data are presented in Appendix 2. The zoning profile of the garnet used for calculations is shown in figure 8d. Rim P-T conditions determined by GARB-GMAP rim thermobarometry.

phic zone, the garnet occasionally contains kyanite inclusions. These observations suggest that part of the garnet growth in sample 55 can be modelled with a As + Grt + Bt + Ms + Pl + Qtz + H_2O assemblage, which has a thermodynamic variance V = 4 in the system $CaO–K_2O–Na_2O–FeO–MnO–MgO–Al_2O_3–SiO_2–H_2O$. Because four independent monitors of compositional changes can be determined from the garnet zoning and the numerous plagioclase inclusions, changes in P-T conditions can be calculated. Analytical procedure and data for the P-T path calculation are summarised in Appendix 2.

The result of thermodynamic modelling (Fig. 9) appears consistent with the phase equilibria constraints on the P-T evolution inferred from the textural analysis. The modelled P-T path corresponds to a clockwise loop suggesting, together with structural data, the following tectonothermal evolution. 1) As a consequence of the underthrusting of the HHC below the Sangla shear zone, sample 55 was buried to a depth of ≈ 30 km (P ≈ 800 MPa) and reached a temperature T ≈ 600–650 °C (Fig. 5, arrow A). 2) When underthrusting ceased, sample 55 underwent isobaric heating from T ≈ 650 to 750 °C (Fig. 5, arrow B and Fig. 9). This stage indicates a relaxation of the geothermal gradient from ≈ 20 to 25 °C/km, most likely as a result of radioactive heating in the thickened crust. Peak metamorphic conditions at T ≈ 750 °C and P ≈ 800 MPa induced anatexis in the upper HHC metapelites through vapor absent melting. 3) The subsequent HHC exhumation was controlled by thrusting along the MCT, erosion, and extension along the SD. The modelled P-T path shows that a significant cooling followed the metamorphic peak and that final equilibration occurred at some stage of the retrograde evolution.

The post peak cooling is rather surprising as thermal models suggest that after the peak of metamorphism, underthrusted rocks should either experience a first period of heating if the exhumation is slow, or follow an isothermal decompression path when the exhumation is rapid (e.g. SPEAR, 1993). Differential re-equilibration of exchange and net-transfer reactions during the retrograde evolution of high-grade rocks can lead to nearly isobaric "pseudo" P-T paths following the dP/dT slope of the net-transfer, pressure sensitive equilibria (FROST and CHACKO, 1989; SELVERSTONE and CHAMBERLAIN, 1990). One has thus to consider the possibility that whereas the GARB exchange reaction recorded cooling, the more sluggish GMAP and GASP net-transfer reactions did not record decompression. Additionally, diffusional re-equilibration at the outer rim of sample 55 garnet may have obliterated the informations about an initial stage of heating during decompression. Several arguments suggest, however, that the retrograde segment of the P-T path is at least semi-quantitatively correct. First, the stability of Ms + Pl + Qtz in the HHC migmatite zone metapelites indicates that significant heating above the calculated peak at T ≈ 750 °C is unlikely (Fig. 5, reaction 12). Second, textural relations show that the retrograde reaction Pl = Grt + Sil + Qtz (= GASP) took place in sample 55 (Fig. 4e), in agreement with a fairly flat cooling path. Third, the absence of low-pressure phases such as cordierite or andalusite suggests no significant decompression. It is worth stressing that in some sections of Nepal, Bhutan, and Zanskar, the metapelites from the uppermost HHC often contain Sil + Crd ± And bearing assemblages, generally interpreted as a consequence of an approximately isothermal decompression caused by extensional tectonic denudation (BRUNEL and KIENAST, 1986; DAVIDSON et al., 1997; DÈZES et al., submitted). The retrograde segment of sample 55 P-T path indicates cooling along a constant geothermal gradient. Such a lack of post-peak thermal relaxation could be the result of two combined processes. First, relaxation could be hindered if the uplift component of the HHC thrusting along the MCT is not balanced by erosion and tectonic denudation. Second, underthrusting of the colder LHC beneath the MCT would tend to lower the geothermal gradient in the HHC.

Discussion

P-T EVOLUTION IN THE SUTLEJ SECTION

The rim thermobarometry results for the staurolite zone at the base of the HHC are consistent with phase equilibria constraints (Figs 6b and 7). Together with the absence of retrograde garnet zoning in this zone (Fig. 8b), these features indicate that the rim P-T estimates reflect peak conditions at T ≈ 580 °C and P ≈ 750 MPa. In contrast, rim thermobarometry results for the HHC kyanite to migmatite zones indicate temperatures that underestimate the P-T stability condition for their characteristic mineral assemblages, as determined from the petrogenetic grid. Although the metamorphic zonation in the HHC implies an up section temperature increase, no clear thermal field gradient can be put in evidence by GARB rim thermometry results. The most likely explanation for this discrepancy is that GARB rim temperatures reflect final equilibration conditions that do not necessarily correspond to the peak of metamorphism. The P-T path calculated for the HHC

migmatitic paragneiss supports this interpretation since it demonstrates that final equilibration, as determined by GARB rim thermometry, occurred at a temperature approximately 150 °C lower than peak conditions. The difference between peak and rim pressures (≈ 220 MPa) suggests that final equilibration occurred after approximately 8 km of exhumation. Although only one sample was suitable for P-T path calculation, the systematic retrograde zoning in the garnets from the HHC kyanite to migmatite zones (Figs 7 and 8) shows that re-equilibration of the GARB thermometer during cooling was a widespread process in the HHC of the Sutlej section. The almost constant equilibration temperature recorded by GARB throughout the HHC is therefore, at least partly, an artefact of re-equilibration during exhumation.

Rim pressure estimates for the HHC sillimanite to migmatite zones also appear to underestimate peak conditions, as deduced from phase equilibria constraints. Although reaction textures suggest that the net-transfer, pressure-sensitive GASP reaction attempted to maintain equilibrium during the retrograde evolution in some samples from the migmatite zone (Fig. 4e), this discrepancy could also reflect the contrasting kinetic behavior of the different thermobarometers (e.g. FROST and CHACKO, 1989). Pressure-sensitive, net-transfer reactions such as the GMAP and GASP barometers re-equilibrate less easily than temperature-sensitive, exchange reaction such as the GARB thermometer. Because the GMAP and GASP equilibria have a positive dP/dT slope, pressure estimates depend on the temperature determinations and are consequently affected by re-equilibration of the thermometer. Such an effect is most likely responsible, at least partly, for the fact that the rim temperature and pressure estimates through the HHC follow a comparable trend, decreasing upward from the staurolite zone to the base of the migmatite zone, and increasing through the migmatite zone, probably reflecting variable re-equilibration in different structural levels.

In contrast to rim P-T estimates, P-T path data for the migmatite zone at the top of the HHC (Fig. 9) indicate a metamorphic peak at T ≈ 750 °C and P ≈ 800 MPa, in agreement with phase equilibria constraints (Fig. 5). Compared to the peak conditions for the staurolite zone at the base of the HHC (T ≈ 580 °C and P ≈ 750 MPa), these results suggest an overall inverted temperature field gradient of ≈ –27 °C/km, whereas peak pressures remain similar within uncertainties suggesting no significant pressure field gradient. Together with the modelled P-T path, these features strongly suggest that the inverted metamorphic field gradient in the HHC is essentially controlled by thermal processes. Because the inverted metamorphic field gradient could be the consequence of diachronic equilibration at different temperatures but more or less constant pressure throughout the sequence, this interpretation does not necessarily imply the existence of an inverted geotherm during the tectonothermal evolution of the HHC.

Rim P-T estimates for the LHC fit, within uncertainties, the phase equilibria constraints for the mineral assemblages characterizing the metamorphic field gradient in this unit (Figs 6a and 7). These results suggest that the metamorphic zonation in the LHC could be the consequence of pressure variations at more or less constant temperature. Retrograde zoning in the garnets from the uppermost LHC sillimanite zone (Figs 7 and 8) indicates, however, that these rocks were also affected to some extent by re-equilibration during cooling.

COMPARISON WITH OTHER HIMALAYAN SECTIONS

Rim thermometry results reveal no clear thermal field gradient in the HHC of the Sutlej section, despite the inverted metamorphic zonation observed in this unit. Such an apparent lack of significant thermal field gradient in the HHC has been already observed in other Himalayan sections. In the Zanskar region of NW Himalaya, an inverted metamorphic field gradient in the HHC is characterized by a superposition of garnet, kyanite + staurolite, sillimanite + muscovite, and sillimanite + K-feldspar zones. Yet, GARB rim temperature estimates through a 30-km-thick section are comprised in the range 550 °C ≤ T ≤ 650 °C, and only a weak thermal field gradient is observed (JAIN and MANICKAVASAGAM, 1993). In the Manaslu region of Nepal, a constant GARB temperature profile at T ≈ 600 °C through a 12-km-thick sequence has been interpreted as the consequence of a thermal buffering caused by widespread, in-situ anatexis (HODGES et al., 1988). A comparable constant temperature profile around T ≈ 605 °C for a 15-km-thick sequence has been determined for the Langtang section (MACFARLANE, 1995). The inverted superposition of kyanite, sillimanite, and sillimanite + K-feldspar zones in this section has been interpreted as the result of diachronic equilibration at different pressures but constant temperature throughout the sequence. This interpretation is based, however, on average temperature determinations and because of the large uncertainties associated (± 100 °C in average) a temperature control cannot be ruled out. Additionally, if final equilibration is likely to have

been reached at different times in distinct levels of the sequence, it is not clear why it occurred at such a uniform temperature.

Anatexis of typical Ms + Pl + Qtz bearing metapelites can begin at T ≈ 650 °C only in water-saturated rocks (THOMPSON and TRACY, 1979). Such a vapor present melting is unlikely to act as a thermal buffer since it is gradually shifted toward higher temperatures as the water is consumed by the reaction. Additionally, Rb/Sr geochemical data indicates that most, if not all, Himalayan leucogranites originated through vapor absent melting (HARRIS et al., 1993). In the Sutlej section, migmatites are restricted to the upper part of the HHC, ruling out a thermal buffering by anatexis throughout the sequence. Although diachronic equilibration at different pressures but constant temperature could be invoked to explain the inverted metamorphic zonation in the Sutlej LHC, thermobarometry results and phase equilibria constraints show that such a process could not explain the range of mineral assemblages observed in the HHC.

On the other hand, several features indicate that the influence of re-equilibration on rim P-T estimates for high-grade rocks are not restricted to the Sutlej section. Retrograde zoning in garnets from high-grade rocks has been observed in several Himalayan sections (INGER and HARRIS, 1992; METCALFE, 1993; MACFARLANE, 1995; VANNAY and HODGES, 1996; DAVIDSON et al., 1997). The GARB thermometry results of JAIN and MANICKAVASAGAM (1993) indicate that the weak thermal field gradient throughout the HHC of Zanskar is partly the consequence of widespread retrograde re-equilibration, and that peak temperatures for sillimanite + K-feldspar zone rocks were up to 100 °C higher than rim estimates. In the Bhagirathi section of Garhwal (Fig. 1), GARB estimates for the sillimanite ± K-feldspar zone at the top of the HHC, and for most of the underlying kyanite zone assemblages, cluster around T ≈ 600 °C, probably recording a late metamorphic stage, in contrast to higher temperatures determined for garnet zone rocks at the base of the sequence (METCALFE, 1993). In Nepal, BRUNEL and KIENAST (1986) noticed that some GARB temperature estimates for sillimanite + cordierite zone rocks at the top of the HHC probably recorded late-metamorphic, cooling conditions. Comparable estimates for sillimanite + K-feldspar zone metapelites from southern Tibet also appear to underestimate peak conditions (HODGES et al., 1993). These observations suggest that the lack of significant thermal field gradient in some Himalayan sections could also be the consequence of re-equilibration during cooling.

PHASE EQUILIBRIA VS THERMOBAROMETRY

Several studies emphasize the potential significance of post-peak re-equilibration in slowly cooled, high-grade metamorphic rocks, and particularly the sensitivity of cation-exchange thermometers to resetting during cooling (e.g. FROST and CHACKO, 1989; SPEAR and FLORENCE, 1992; FITZSIMONS and HARLEY, 1994). Such thermometers may be unable to record peak temperatures if these latter are higher than the "closure temperature" of the reaction, that is the temperature at which diffusion ceases. For example, modelling of diffusion in garnet suggests that it may be very difficult to calculate peak conditions using GARB rim thermometry on amphibolite facies rocks (T max. > 550 °C; SPEAR, 1991). Because it is a function not only of the cooling rate and grain size, but also of deformation and/or fluids, the closure temperature of a reaction can be variable. Consequently, FROST and CHACKO (1989) suggested that the temperatures produced by thermometers for natural systems can allow an empirical estimate of their closure temperatures. Our rim thermometry results suggest an average closure temperature around T ≈ 570 °C for the GARB thermometer in the HHC of the studied section.

In high-grade rocks from the Sutlej and other sections, rim P-T estimates obtained with several independent thermobarometers for the same rock are often consistent and suggest well-equilibrated systems, even if peak conditions appear to be underestimated. This feature implies that the potential effect of re-equilibrations may not be readily assessed on the basis of the thermobarometry results only, emphasizing the need to use other independent arguments for this purpose. Because the composition of the phase rims is more easily modified by re-equilibration, the core composition of zoned garnets is occasionally used together with the composition of matrix phases in order to calculate simple core-to-rim P-T trends and approach peak conditions (e.g. METCALFE, 1993). This procedure, relying on the unwarranted assumption that the garnet cores are in equilibrium with matrix phases, has two major drawbacks. If re-equilibration took place only through exchange reactions, the calculated temperatures can approach, but still underestimate, peak conditions (SPEAR and FLORENCE, 1992; SPEAR, 1993), but incorrect "pseudo" P-T path following the dP/dT slope of the net-transfer barometer reactions will be determined (SELVERSTONE and CHAMBERLAIN, 1990). If re-equilibration occurred through both exchange and net-transfer reactions, P-T estimates can significantly overestimate peak conditions (SPEAR and FLORENCE, 1992; SPEAR, 1993).

This is indeed the case for the Sutlej section rocks. Using the core composition at lowest Fe/(Fe + Mg) ratio for garnets showing retrograde zoning, together with matrix phase compositions, P-T estimates for the upper LHC sillimanite zone (sample 16) and for the HHC kyanite to migmatite zones (samples 59, 60, and 62) plot above the vapor absent melting reaction (Fig. 5, reaction 11) although these rocks do not contain evidences for anatexis. Three HHC samples (samples 50, 57, and 62) even plot above the upper stability for Ms + Pl + Qtz (Fig. 5, reaction 12) although this sub-assemblage is present throughout the unit. Together with the reaction textures and P-T path data, these results suggest that the mineral assemblages attempted to maintain equilibrium with respect to changing P-T conditions through both exchange and net-transfer reactions during the retrograde evolution.

Although re-equilibrations modified the composition of solid solution phases, peak metamorphic mineral assemblages are generally preserved and peak conditions can be inferred from a petrogenetic grid. Using such an approach, DAVIDSON et al. (1997) recently demonstrate that the HHC of Bhutan experienced decompression while maintaining a laterally heterogeneous, and locally inverted, internal temperature range of T ≈ 600 to 750 °C. They also argue that widespread retrograde zoning at the rim of garnets suggests that GARB rim estimates reflect closure temperatures. From these results, these authors express concerns comparable to ours about the ability of rim thermobarometry to provide reliable constraints allowing to test models for the inverted metamorphism.

Conclusions

An inverted metamorphic field gradient is observed in most sections across the crystalline core of the Himalayan orogen. To place quantitative constraints on the P-T conditions associated with this metamorphic zonation, several studies applied thermobarometry method on metapelitic rocks. In some sections, garnet-biotite rim thermometry determinations put in evidence inverted temperature field gradients in the MCT zone at the base of the HHC (e.g. HUBBARD, 1989; PÊCHER, 1989; METCALFE, 1993). Yet, several studies reveal that the rocks throughout the HHC of some Himalayan sections reached final equilibration at an approximately uniform temperature around T ≈ 600 °C. These results suggest that the inverted metamorphism in the HHC is not necessarily controlled by thermal processes and it has been proposed that it represents mainly the consequence of diachronic equilibration at different pressures but constant temperature (MACFARLANE, 1995). To explain the apparent lack of temperature field gradient, HODGES et al. (1988) invoked a thermal buffering caused by anatexis.

In contrast, new data from the HHC of the Sutlej section suggest that the inverted metamorphic field gradient from the base to the top of this unit is associated with an up section increase in peak temperature from T ≈ 580 °C to T ≈ 750 °C at an approximately constant pressure P ≈ 750–800 MPa. Together with PT path data, these results suggest that the inverted metamorphic field gradient in the HHC is the consequence of diachronic equilibration at different temperatures but more or less constant pressure throughout the sequence. Rim thermobarometry indicates, however, that final equilibration throughout the HHC occurred at an approximately constant temperature around T ≈ 570 °C. P-T path and garnet zoning data demonstrate that the discrepancy between peak conditions and rim P-T estimates for the kyanite to migmatite zones is the consequence of retrograde re-equilibrations. Rocks from different structural levels in the HHC most probably reached final equilibration at different times during exhumation as they cooled below the closure temperature for the garnet-biotite thermometer. The apparent lack of temperature field gradient in the Sutlej HHC reflects thus a limitation of the thermobarometry method and not a real tectonothermal process. Discrepancies between phase equilibria constraints and rim thermobarometry data for high-grade rocks from other Himalayan sections suggest that re-equilibrations hindered, to some extent, the ability of rim thermometry methods to constrain the peak thermal structure of the Himalayan orogen. The potential significance of retrograde re-equilibrations should be thus assessed critically before using quantitative P-T estimates as a basis for interpreting and modelling the Himalayan tectonothermal evolution.

Acknowledgements

We thank Maria-Letizia Filippi and Matthieu Girard for assisting with field work, Georges Mascle for helping with sample transport, Raymond Ansermoz and Laurent Nicod for preparation of thin and polished sections, Francois Bussy for supervising microprobe work, Philippe Thélin for XRD determinations, Wolfgang Frank and Albrecht Steck for fruitful discussions, Pierre Dèzes, Martin Frey, and Patrick LeFort for reviewing the manuscript. J.-C. V. and B.G. acknowledge support from the Swiss National Science Foundation (FNRS grants

20-38917.93 and 20-45063.95, director A. Steck) and from the Austrian "Fonds zur Förderung der wissenschaftlichen Forschung" (FWF grant p-11765-geo).

References

BERMAN, R.G. (1990): Mixing properties of Ca–Mg–Fe–Mn garnets. Amer. Mineralogist 75, 328–344.

BERMAN, R.G. (1991): Thermobarometry using multi-equilibrium calculations: a new technique with petrologic applications. Canad. Mineralogist 29, 833–855.

BERTHELSEN, A. (1951): A geological section through the Himalayas. Medd. Dansk geol. Foren. 12, 102–104.

BHAT, M.I. and LEFORT, P. (1992): Sm–Nd age and petrogenesis of Rampur metavolcanic rocks, NW Himalayas: Late Archean relics in the Himalayan belt. Precambrian Res. 56, 191–210.

BRUNEL, M. and KIENAST, J.-R. (1986): Etude pétrostructurale des chevauchements ductiles himalayens sur la transversale de l'Everest-Makalu (Népal oriental). Canad. J. Earth Sci. 23, 1117–1137.

CHATTERJEE, N.D. and FLUX, S. (1986): Thermodynamic mixing properties of muscovite-paragonite crystalline solutions at high temperatures and pressures, and their geological applications. J. Petrol. 27, 677–693.

DAVIDSON, C., GRUJIC, D.E., HOLLISTER, L.S. and SCHMID, S. M. (1997): Metamorphic reactions related to decompression and synkinematic intrusion of leucogranite, High Himalayan Crystallines, Bhutan. J. Metamorphic Geol. 15, 593–612.

DÈZES, P.J. VANNAY, J.C., STECK, A., BUSSY, F. and COSCA, M. (submitted): Synorogenic extension; quantitative constraints on the age and throw of the Zanskar Shear Zone (NW Himalaya). Bull. Geol. Soc. Amer.

ELKINS, L.T. and GROVE, T.L. (1990): Ternary feldspar experiments and thermodynamic models. Amer. Mineralogist 75, 544–559.

FITZSIMONS, I.C.W. and HARLEY, S.L. (1994): The influence of retrograde cation exchange on granulite P-T estimates and a convergence technique for recovery of peak metamorphic conditions. J. Petrol. 35/2, 543–576.

FRANK, W., GRASEMANN, B., GUNTLI, P. and MILLER, C. (1995): Geological map of the Kishtwar-Chamba-Kulu region (NW Himalayas, India). Jb. geol. Bundesanst. (Wien) 138/2, 299–308.

FRANK, W., THÖNI, M. and PURTSCHELLER, F. (1977): Geology and petrography of Kulu-South Lahul area. Colloq. int. CNRS (Paris) 268, 147–160.

FROST, B.R. and CHACKO, T. (1989): The granulite uncertainty principle: limitations on thermobarometry in granulites. J. Geol. 97, 435–450.

GURURAJAN, N.S. (1994): Porphyroblasts-matrix microstructural relationships from the Crystalline Thrust Sheets of Satluj valley, Himachal Pradesh. J. geol. Soc. India 44, 367–379.

HARRIS, N., INGER, S. and MASSEY, J. (1993): The role of fluids in the formation of High Himalayan leucogranites. In: TRELOAR, P.J. and SEARLE, M.P. (eds): Himalayan Tectonics (p. 391–400). Geol. Soc. Spec. Publ. (London) 74.

HERREN, E. (1987): Zanskar shear zone: Northeast–southwest extension within the Higher Himalayas (Ladakh, India). Geology 15, 409–413.

HODGES, K.V., BURCHFIEL, B.C., ROYDEN, L.H., CHEN, Z. and LIU, Y. (1993): The metamorphic signature of contemporaneous extension and shortening in the central Himalayan orogen: data from the Nyalam transect, southern Tibet. J. Metamorphic Geol. 11, 721–737.

HODGES, K.V., LEFORT, P. and PÊCHER, A. (1988): Possible thermal buffering by crustal anatexis in collisional orogens: thermobarometric evidence from the Nepalese Himalaya. Geology 16, 707–710.

HODGES, K.V. and MCKENNA, L.W. (1987): Realistic propagation of uncertainties in geologic thermobarometry. Amer. Mineralogist 72, 671–680.

HODGES, K.V., PARRISH, R.R., HOUSH, T.B., LUX, D.R., BURCHFIEL, B.C., ROYDEN, L.H. and CHEN, Z. (1992): Simultaneous Miocene extension and shortening in the Himalayan Orogen. Science 258, 1466–1469.

HODGES, K.V. and SILVERBERG, D.S. (1988): Thermal evolution of the Greater Himalaya, Garhwal, India. Tectonics 7/3, 583–600.

HUBBARD, M.S. (1989): Thermobarometric constraints on the thermal history of the Main Central Thrust Zone and Tibetan Slab, eastern Nepal Himalaya. J. Metamorphic Geol. 7, 19–30.

HUBBARD, M.S. and HARRISON, T.M. (1989): $^{40}Ar/^{39}Ar$ age constraints on deformation and metamorphism in the Main Central Thrust Zone and Tibetan Slab, eastern Nepal Himalaya. Tectonics 8/4, 865–880.

INGER, S. and HARRIS, N.B.W. (1992): Tectonothermal evolution of the High Himalayan Crystalline Sequence, Langtang Valley, northern Nepal. J. Metamorphic Geol. 10, 439–452.

JAIN, A.K. and ANAND, A. (1988): Deformation and strain patterns of an intracontinental collision ductile shear zone – an example from the Higher Garhwal Himalaya. J. struct. Geol. 10/7, 717–734.

JAIN, A.K. and MANICKAVASAGAM, R.M. (1993): Inverted metamorphism in the intracontinental ductile shear zone during Himalayan collision tectonics. Geology 21, 407–410.

JAMIESON, R.A., BEAUMONT, C., HAMILTON, J.K. and FULLSACK, P. (1996): Tectonic assembly of inverted metamorphic sequences. Geology 24–9, 839–842.

KAKAR, R.K. (1988): Geology and tectonic setting of Central Crystalline rocks of southern part of Higher Himachal Himalaya. J. geol. Soc. India 31, 243–250.

KOHN, M.J., SPEAR, F.S. and DALZIEL, I.W.D. (1993): Metamorphic P-T paths from Cordillera Darwin, a core complex in Tierra del Fuego, Chile. J. Petrol. 34/3, 519–542.

KRETZ, R. (1983): Symbols for rock-forming minerals. Amer. Mineralogist 68, 277–279.

KWATRA, S.K., BHANOT, V.B., KAKAR, R.K. and KANSAL, A.K. (1986): Rb–Sr radiometric ages of the Wangtu Gneissic Complex, Kinnaur district, Higher Himachal Himalaya. Bull. Indian Geol. Assoc. 19/2, 127–130.

LEBRETON, N. and THOMPSON, A.B. (1988): Fluid-absent (dehydration) melting of biotite in metapelites in the early stages of crustal anatexis. Contr. Mineral. Petrol. 99, 226–237.

MACFARLANE, A.M. (1995): An evaluation of the inverted metamorphic gradient at Langtang National Park, central Nepal Himalaya. J. Metamorphic Geol. 13, 595–612.

MALLET, F.R. (1875): On the geology and mineral ressources of the Darjiling district and the western Duars. Mem. Geol. Surv. India 11, 1–50.

MCKENNA, L.W. and HODGES, K.V. (1988): Accuracy versus precision in locating reaction boundaries: Implications for the garnet-plagioclase-aluminium sili-

cate-quartz geobarometer. Amer. Mineralogist 73, 1205–1208.

METCALFE, R.P. (1993): Pressure, temperature and time constraints on metamorphism across the Main Central Thrust zone and High Himalayan Slab in the Garhwal Himalaya. In: TRELOAR, P.J. and SEARLE, M.P. (eds): Himalayan Tectonics (p. 485–509). Geol. Soc. Spec. Publ. (London) 74.

MISRA, D.K. (1993): Tectonic setting and deformational features in Satluj and Beas valley of Himachal Pradesh. Indian J. Petroleum Geol. 2/1, 81–92.

NEWTON, R.C., CHARLU, T.B. and KLEPPA, O.J. (1980): Thermochemistry of the high structural state plagioclases. Geochim. Cosmochim. Acta 44, 933–941.

PATEL, R.C., SINGH, S., ASOKAN, A., MANICKAVASAGAM, R.M. and JAIN, A.K. (1993): Extensional tectonics in the Himalayan orogen, Zanskar, NW India. In: TRELOAR, P.J. and SEARLE, M.P. (eds): Himalayan Tectonics (p. 445–459). Geol. Soc. Spec. Publ. (London) 74.

PATIÑO DOUCE, A.E., JOHNSTON, A.D. and RICE, J.M. (1993): Octaedral excess mixing properties in biotite: a working model with applications to geobarometry and geothermometry. Amer. Mineralogist 78, 113–131.

PÊCHER, A. (1989): The metamorphism in the central Himalaya. J. Metamorphic Geol. 7, 31–41.

PÊCHER, A. and SCAILLET, B. (1989): La structure du Haut-Himalaya au Garhwal (Indes). Eclogae geol. Helv. 82/2, 655–668.

SELVERSTONE, J. and CHAMBERLAIN, C.P. (1990): Apparent isobaric cooling paths from granulites: two counterexamples from British Columbia and New Hampshire. Geology 18, 307–310.

SHARMA, K.K. (1977): A contribution to the geology of the Sutluj valley, Kinnaur, Himachal Pradesh, India. Colloq. int. CNRS (Paris) 268, 369–379.

SINGH, S. and JAIN, A.K. (1993): Deformational and strain patterns of the Jutogh Nappe along the Sutlej valley in Jeori-Wangtu region, Himachal Pradesh, India. J. Himalayan Geol. 4, 41–55.

SPEAR, F.S. (1991): On the interpretation of peak metamorphic temperatures in light of garnet diffusion during cooling. J. Metamorphic Geol. 9, 379–388.

SPEAR, F.S. (1993): Metamorphic phase equilibria and Pressure-Temperature-Time paths. Mineralogical Society of America, Washington D. C.

SPEAR, F.S. and FLORENCE, F.P. (1992): Thermobarometry in granulites: pitfalls and new approaches. Precambrian Res. 55, 209–241.

SPEAR, F.S. and SELVERSTONE, J. (1983): Quantitative P-T paths from zoned minerals: theory and tectonic applications. Contr. Mineral. Petrol. 83, 348–357.

SWAPP, S.M. and HOLLISTER, L.S. (1991): Inverted metamorphism within the Tibetan Slab of Bhutan: evidence for a tectonically transported heat-source. Canad. Mineralogist 29, 1019–1041.

TEWARI, A.P., GAUR, R.K. and AMETA, S.S. (1978): A note on the geology of a part of Kinnaur district, Himachal Pradesh. Himalayan Geol. 8/1, 574–582.

THOMPSON, A.B. and TRACY, R.J. (1979): Model systems for anatexis of pelitic rocks: facies series melting and reactions in the system CaO–$KAlO_2$–$NaAlO_2$–Al_2O_3–SiO_2–H_2O. Contr. Mineral. Petrol. 70, 29–438.

VALDIYA, K.S. (1981): Tectonics of the central sector of the Himalaya. In: GUPTA, H.K. and DELANY, F.M. (eds): Zagros-Hindu Kush-Himalaya geodynamic evolution. Geodynamic Series 3, 87–110.

VANNAY, J.C. and HODGES, K.V. (1996): Tectonometamorphic evolution of the Himalayan metamorphic core between the Annapurna and Dhaulagiri, central Nepal. J. Metamorphic Geol. 14, 635–656.

Received September 29, 1997; revision accepted January 6, 1998.

Appendix

1. THERMOBAROMETRY ANALYTICAL PROCEDURE

The analytical procedure used for geothermobarometry follows the approach presented in HODGES and MCKENNA (1987) and HODGES et al. (1993). At least two domains where the relevant mineral phases are in sharp contacts were selected in each polished section. For rim geothermobarometry, mineral compositions were measured along the contacts using the Cameca SX50 electron microprobe at the University of Lausanne. The acceleration voltage was 15 kV for all phases and the nominal beam current was 25 nA for garnet, 15 nA for biotite and muscovite, and 10 nA for plagioclase. To take in account the variations in chemical composition in the mineral phases, an average of 15 analyses was performed for biotite, muscovite, and plagioclase in each sample. For garnet, an average of 23 measurements was taken. Average rim compositions are presented in tables A3 to A6. The standard deviations of these analyses reflect the analytical uncertainties, as well as imperfect equilibria. Rim pressures and temperatures have been calculated with a computer program written by K.V. Hodges (MacPT), using the thermobarometers and calibrations listed in table A2. The uncertainties on the P–T estimates have been calculated by propagation of the initial standard deviations through the geothermobarometric equations, using a Monte Carlo approach. These uncertainties correspond to ellipses in P-T space and represent a measure of the precision of the P-T estimates and not of their accuracy, as calibrations and activity model uncertainties are not considered. The equilibration state of the studied assemblages was also tested through multiple equilibria calculations performed with the ther-

modynamic data base and computer program (TWQ 1.02) of BERMAN (1991). Because different activity models and calibrations are used, the absolute P-T estimates calculated with both methods are not directly comparable. Yet, differences in the pressure and temperature recorded by one sample relative to another remain comparable when calculated with both methods.

2. THERMODYNAMIC MODELLING ANALYTICAL PROCEDURE

The theoretical bases of thermodynamic modelling are presented in SPEAR and SELVERSTONE (1983) and SPEAR (1993). For the analytical procedure, we followed the approach presented by KOHN et al. (1993). The four differential parameters required to monitor P-T changes in sample 55 were determined from the almandine, spessartine, and grossular phase components of the zoned garnet, as well as from the anorthite component of plagioclase inclusions. Several analyses of plagioclase inclusions and of the surrounding garnet were performed along the garnet composition profile presented in figure 8d. Because the outermost rim of the garnet shows a retrograde zoning, inclusions from this domain have not been considered. No significant local zoning was observed in, and around, the analysed inclusions. The good correlation between the relative position of the plagioclase inclusions within the garnet, the garnet composition around them, and the overall garnet zoning, allowed to determine the progressive composition changes listed in table A7. From these data, P-T changes were calculated using a computer program written by F. Spear (Program Gibbs).

Tab. A1 Summary of mineral assemblages*.

Metapelites: Bt + Ms + Pl + Qtz +							
Mrg	Chl	Grt	St	Ky	Sil	Kfs	Samples
x	x	x	-	-	-	-	10,11,31
-	x	x	-	-	-	-	2,22,24,63,67,84,85, 32–34,39
-	±	x	-	-	-	-	25,28,36,37,61,65,66,74,82
-	±	x	x	-	-	-	26,73
-	±	-	x	-	-	-	12
-	-	x	x	x	-	-	40
-	-	x	-	x	-	-	27,62,70
-	-	±	x	x	x	-	76,83
-	-	x	x	-	x	-	16,75,81
-	-	x	-	-	x	-	56
-	-	x	-	x	x	-	14,57–60
-	-	x	-	x	x	±	48–50,54,55
-	-	x	-	-	-	x	46,47,52,69
Metabasites: Pl + Qtz +							
Chl	Ep	Act	Hbl	Grt	Cpx	Bt	Samples
x	x	-	-	-	-	-	4
x	x	x	-	-	-	x	1,5,6
x	±	-	x	-	-	x	7,9,86
-	-	-	x	-	-	x	13,15,17,18,20
-	-	-	x	x	-	x	53,64
-	-	-	x	±	x	±	41,51,71,72

* Mineral abbreviations after KRETZ (1983).

Tab. A2 Thermobarometers.

Acronym	Reaction
GARB	Grt (alm) + Bt (phl) = Grt (prp) + Bt (ann)
GASP	Grt (grs) + As + Qtz = Pl (an)
GMAP	Grt (alm) + Grt (grs) + Ms = Pl (an) + Bt (ann)
GRAIL	Grt (alm) + Rt = Ilm + As + Qtz

Solution models for garnet, biotite, muscovite and plagioclase after BERMAN (1990), PATIÑO DOUCE et al. (1993), CHATTERJEE and FLUX (1986), and ELKINS and GROVE (1990), respectively. Calibrations for GARB, GMAP, and GRAIL after HODGES and MCKENNA (1987), and after MCKENNA and HODGES (1988) for GASP.

Tab. A7 Gibbs modelling P-T path data for sample 55.

Assemblage: Grt+Bt+As+Ms+Pl+Qtz+H_2O System: CaO-K_2O-Na_2O-FeO-MnO-MgO-Al_2O_3-SiO_2-H_2O					
ΔX_{alm}	ΔX_{sps}	ΔX_{grs}	ΔX_{an}	ΔT [°C]	ΔP [MPa]
0.024	–0.111	0.039	0.275	170	221
0.008	–0.015	0.006	0.036	–2	14
–0.010	0.015	–0.015	–0.144	8	21
0.010	–0.015	0.016	0.053	–36	–12
0.004	0.009	–0.008	–0.059	–15	–21
–0.007	–0.009	0.023	0.084	–24	7
–0.019	0.012	0.015	0.077	–23	–14

Activity models for Grt, Ms, and Pl after BERMAN (1990), CHATTERJEE and FLUX (1986), and NEWTON et al. (1980). Deltas (Δ) correspond to changes relative to previous increment, starting with rim conditions, and listed from rim to core. For monitors, ΔX_{alm}, ΔX_{sps}, and ΔX_{grs} are changes in molar fractions derived from rim-core garnet zoning. ΔX_{an} are derived from plagioclase inclusions, and from matrix plagioclase for the first step. See tables A3 and A6 for rim compositions.

Tab. A3 Garnet rim compositions (12 O basis).

Sample	16	33	39	40	48	49	50	52	54	55	56	57
SiO_2	36.72 ± 0.13	36.90 ± 0.12	36.84 ± 0.15	37.09 ± 0.13	37.06 ± 0.12	36.85 ± 0.20	36.69 ± 0.12	36.65 ± 0.17	36.76 ± 0.13	36.94 ± 0.11	36.86 ± 0.11	36.96 ± 0.10
TiO_2	0.04 ± 0.01	0.02 ± 0.01	0.01 ± 0.01	0.05 ± 0.02	0.03 ± 0.02	0.05 ± 0.02	0.04 ± 0.02	0.03 ± 0.02	0.04 ± 0.02	0.03 ± 0.01	0.03 ± 0.02	0.03 ± 0.01
Al_2O_3	20.88 ± 0.09	21.05 ± 0.12	21.01 ± 0.11	21.19 ± 0.08	21.05 ± 0.12	20.88 ± 0.12	20.95 ± 0.07	20.79 ± 0.09	20.97 ± 0.17	21.06 ± 0.07	20.96 ± 0.09	21.05 ± 0.13
FeO	36.97 ± 0.17	34.17 ± 0.19	33.01 ± 0.14	33.74 ± 0.32	32.26 ± 0.25	34.93 ± 0.14	35.05 ± 0.18	37.53 ± 0.36	30.78 ± 0.21	31.44 ± 0.28	32.49 ± 0.38	33.65 ± 0.28
MnO	2.02 ± 0.12	4.33 ± 0.27	6.49 ± 0.15	2.66 ± 0.59	5.74 ± 0.43	3.69 ± 0.16	4.99 ± 0.25	3.29 ± 0.17	8.24 ± 0.36	7.03 ± 0.26	6.75 ± 0.35	5.48 ± 0.42
MgO	1.97 ± 0.09	2.18 ± 0.13	2.41 ± 0.08	3.12 ± 0.19	2.79 ± 0.16	2.31 ± 0.12	2.36 ± 0.13	1.27 ± 0.07	2.54 ± 0.16	2.68 ± 0.16	2.43 ± 0.08	2.71 ± 0.16
CaO	2.07 ± 0.10	2.23 ± 0.20	0.91 ± 0.03	2.97 ± 0.24	1.92 ± 0.25	2.00 ± 0.19	0.79 ± 0.06	1.48 ± 0.09	1.30 ± 0.05	1.71 ± 0.18	1.30 ± 0.07	1.18 ± 0.08
Cr_2O_3	0.01 ± 0.01	0.01 ± 0.01	0.01 ± 0.01	0.02 ± 0.01	0.01 ± 0.01	0.02 ± 0.01	0.01 ± 0.01	0.01 ± 0.01	0.02 ± 0.01	0.01 ± 0.01	0.01 ± 0.01	0.02 ± 0.01
Total	100.68 ± 0.29	100.89 ± 0.21	100.69 ± 0.27	100.84 ± 0.27	100.86 ± 0.23	100.73 ± 0.43	100.88 ± 0.22	101.06 ± 0.38	100.64 ± 0.25	100.91 ± 0.19	100.85 ± 0.34	101.08 ± 0.18
Si	2.97	2.97	2.98	2.97	2.98	2.98	2.97	2.98	2.97	2.97	2.97	2.97
Ti	0.00	0.00	0.00	0.00	0.00	0.00	0.00	0.00	0.00	0.00	0.00	0.00
Al	1.99	2.00	2.00	2.00	1.99	1.99	2.00	1.99	2.00	2.00	1.99	1.99
Fe	2.50	2.30	2.23	2.26	2.17	2.36	2.37	2.55	2.08	2.11	2.19	2.26
Mn	0.14	0.30	0.44	0.18	0.39	0.25	0.34	0.23	0.56	0.48	0.46	0.37
Mg	0.24	0.26	0.29	0.37	0.33	0.28	0.28	0.15	0.31	0.32	0.29	0.33
Ca	0.18	0.19	0.08	0.25	0.17	0.17	0.07	0.13	0.11	0.15	0.11	0.10
Cr	0.00	0.00	0.00	0.00	0.00	0.00	0.00	0.00	0.00	0.00	0.00	0.00
Sum	8.03	8.03	8.02	8.03	8.03	8.03	8.03	8.03	8.03	8.03	8.03	8.03
n	27	26	22	30	25	22	27	24	27	24	20	26

Sample	59	60	62	63	65	66	73	76	81	82	84	85
SiO_2	36.84 ± 0.09	36.92 ± 0.10	37.00 ± 0.12	36.75 ± 0.10	36.78 ± 0.25	36.88 ± 0.12	37.02 ± 0.33	37.14 ± 0.12	36.80 ± 0.12	36.73 ± 0.13	37.22 ± 0.21	37.00 ± 0.17
TiO_2	0.02 ± 0.01	0.03 ± 0.01	0.12 ± 0.27	0.04 ± 0.02	0.04 ± 0.02	0.03 ± 0.01	0.03 ± 0.01	0.07 ± 0.03	0.04 ± 0.03	0.04 ± 0.01	0.09 ± 0.03	0.04 ± 0.02
Al_2O_3	21.02 ± 0.08	21.04 ± 0.05	21.06 ± 0.07	20.87 ± 0.08	20.84 ± 0.16	20.97 ± 0.07	21.03 ± 0.13	21.04 ± 0.06	20.85 ± 0.12	20.84 ± 0.14	21.11 ± 0.10	21.16 ± 0.10
FeO	32.41 ± 0.15	32.53 ± 0.17	33.40 ± 0.22	29.49 ± 0.30	36.76 ± 0.44	29.87 ± 0.49	37.28 ± 0.68	34.12 ± 0.55	35.75 ± 0.38	28.82 ± 0.32	33.41 ± 0.65	31.96 ± 0.54
MnO	6.61 ± 0.30	6.53 ± 0.25	4.81 ± 0.26	8.39 ± 0.41	1.29 ± 0.63	8.56 ± 0.78	0.94 ± 0.15	0.88 ± 0.41	2.73 ± 0.13	10.04 ± 0.27	0.81 ± 0.27	3.33 ± 0.40
MgO	2.73 ± 0.14	2.62 ± 0.11	2.75 ± 0.19	1.39 ± 0.09	2.21 ± 0.18	1.86 ± 0.17	2.09 ± 0.19	2.06 ± 0.12	2.14 ± 0.07	1.10 ± 0.04	1.46 ± 0.11	1.49 ± 0.08
CaO	1.20 ± 0.04	1.20 ± 0.06	1.73 ± 0.24	3.69 ± 0.12	2.71 ± 0.17	2.77 ± 0.40	2.28 ± 0.38	5.42 ± 0.55	2.25 ± 0.29	3.23 ± 0.15	6.72 ± 0.66	5.71 ± 0.46
Cr_2O_3	0.01 ± 0.01	0.01 ± 0.01	0.02 ± 0.02	0.02 ± 0.01	0.02 ± 0.02	0.01 ± 0.01	0.02 ± 0.01	0.02 ± 0.01	0.02 ± 0.01	0.01 ± 0.01	0.03 ± 0.02	0.02 ± 0.01
Total	100.86 ± 0.16	100.88 ± 0.18	100.89 ± 0.32	100.63 ± 0.20	100.65 ± 0.55	100.96 ± 0.24	100.69 ± 0.25	100.74 ± 0.17	100.58 ± 0.25	100.81 ± 0.40	100.84 ± 0.27	100.72 ± 0.25
Si	2.97	2.97	2.97	2.97	2.97	2.97	2.99	2.98	2.98	2.98	2.98	2.97
Ti	0.00	0.00	0.01	0.00	0.00	0.00	0.00	0.00	0.00	0.00	0.01	0.00
Al	2.00	2.00	1.99	1.99	1.98	1.99	2.00	1.99	1.99	1.99	1.99	2.00
Fe	2.18	2.19	2.24	2.00	2.48	2.01	2.51	2.29	2.42	1.95	2.24	2.15
Mn	0.45	0.45	0.33	0.57	0.09	0.58	0.06	0.06	0.19	0.69	0.05	0.23
Mg	0.33	0.31	0.33	0.17	0.27	0.22	0.25	0.25	0.26	0.13	0.17	0.18
Ca	0.10	0.10	0.15	0.32	0.24	0.24	0.20	0.47	0.19	0.28	0.58	0.49
Cr	0.00	0.00	0.00	0.00	0.00	0.00	0.00	0.00	0.00	0.00	0.00	0.00
Sum	8.03	8.03	8.02	8.03	8.03	8.03	8.01	8.03	8.03	8.03	8.02	8.02
n	22	28	20	23	23	20	20	21	24	24	22	22

Note: Average mineral rim compositions, based on n analyses. Uncertainties are quoted at the 1σ confidence level.

Tab. A4 Biotite rim compositions (11 O basis).

Sample	16	33	39	40	48	49	50	52	54	55	56	57
SiO_2	34.72 ± 0.25	35.62 ± 0.30	36.06 ± 0.13	36.37 ± 0.35	34.84 ± 0.33	35.25 ± 0.24	34.48 ± 0.26	34.13 ± 0.24	34.92 ± 0.76	35.36 ± 0.20	34.96 ± 0.26	35.78 ± 0.22
TiO_2	2.19 ± 0.16	1.37 ± 0.11	1.52 ± 0.06	1.60 ± 0.12	2.59 ± 0.12	2.95 ± 0.43	3.19 ± 0.26	2.34 ± 0.28	2.79 ± 0.16	2.11 ± 0.15	2.32 ± 0.38	2.23 ± 0.14
Al_2O_3	19.22 ± 0.19	18.80 ± 0.27	19.25 ± 0.09	19.99 ± 0.31	19.64 ± 0.31	19.15 ± 0.34	18.99 ± 0.25	19.49 ± 0.41	19.09 ± 0.28	19.70 ± 0.22	20.00 ± 0.36	19.69 ± 0.19
FeO	22.74 ± 0.47	20.78 ± 0.39	19.46 ± 0.48	17.14 ± 0.58	18.86 ± 0.37	21.13 ± 0.40	21.10 ± 0.39	23.18 ± 0.23	19.04 ± 0.43	18.67 ± 0.23	18.60 ± 0.29	18.33 ± 0.23
MnO	0.08 ± 0.03	0.12 ± 0.03	0.11 ± 0.04	0.08 ± 0.03	0.15 ± 0.03	0.10 ± 0.03	0.17 ± 0.04	0.09 ± 0.03	0.28 ± 0.06	0.20 ± 0.05	0.16 ± 0.08	0.12 ± 0.03
MgO	7.56 ± 0.23	9.55 ± 0.20	10.43 ± 0.17	11.36 ± 0.14	9.66 ± 0.10	8.18 ± 0.21	8.09 ± 0.18	6.41 ± 0.12	9.35 ± 0.13	9.81 ± 0.19	9.39 ± 0.24	10.28 ± 0.16
CaO	0.02 ± 0.03	0.01 ± 0.01	0.02 ± 0.02	0.02 ± 0.01	0.00 ± 0.00	0.02 ± 0.02	0.00 ± 0.00	0.00 ± 0.00	0.01 ± 0.01	0.01 ± 0.01	0.00 ± 0.00	0.01 ± 0.01
Na_2O	0.61 ± 0.12	0.79 ± 0.10	0.25 ± 0.02	1.15 ± 0.11	0.21 ± 0.02	0.51 ± 0.05	0.21 ± 0.04	0.07 ± 0.01	0.76 ± 0.15	0.69 ± 0.08	0.18 ± 0.03	0.74 ± 0.08
K_2O	9.19 ± 0.22	9.12 ± 0.28	9.08 ± 0.12	8.78 ± 0.11	9.56 ± 0.07	9.30 ± 0.10	9.30 ± 0.10	9.60 ± 0.10	9.37 ± 0.12	9.40 ± 0.13	9.67 ± 0.20	9.31 ± 0.11
F	0.55 ± 0.05	0.24 ± 0.02	0.23 ± 0.03	0.28 ± 0.02	0.30 ± 0.05	0.29 ± 0.03	0.40 ± 0.03	0.68 ± 0.04	0.22 ± 0.02	0.27 ± 0.03	0.23 ± 0.02	0.25 ± 0.03
Total	96.87 ± 0.41	96.42 ± 0.48	96.41 ± 0.34	96.77 ± 0.24	95.80 ± 0.43	96.88 ± 0.39	95.94 ± 0.43	95.98 ± 0.23	95.82 ± 1.26	96.22 ± 0.34	95.51 ± 0.43	96.74 ± 0.26
Si	2.66	2.70	2.71	2.69	2.64	2.67	2.65	2.65	2.66	2.67	2.66	2.67
Ti	0.13	0.08	0.09	0.09	0.15	0.17	0.18	0.14	0.16	0.12	0.13	0.13
Al	1.74	1.68	1.70	1.74	1.76	1.71	1.72	1.79	1.71	1.75	1.79	1.73
Fe	1.46	1.32	1.22	1.06	1.20	1.34	1.35	1.51	1.21	1.18	1.18	1.15
Mn	0.01	0.01	0.01	0.00	0.01	0.01	0.01	0.01	0.02	0.01	0.01	0.01
Mg	0.86	1.08	1.17	1.25	1.09	0.92	0.93	0.74	1.06	1.10	1.06	1.15
Ca	0.00	0.00	0.00	0.00	0.00	0.00	0.00	0.00	0.00	0.00	0.00	0.00
Na	0.09	0.12	0.04	0.17	0.03	0.07	0.03	0.01	0.11	0.10	0.03	0.11
K	0.90	0.88	0.87	0.83	0.93	0.90	0.91	0.95	0.91	0.91	0.94	0.89
F	0.13	0.06	0.05	0.07	0.07	0.07	0.10	0.17	0.05	0.06	0.06	0.06
Sum	7.84	7.88	7.81	7.84	7.81	7.79	7.78	7.80	7.84	7.84	7.80	7.83
n	17	12	13	17	12	15	13	17	16	14	13	16

Sample	59	60	62	63	65	66	73	76	81	82	84	85
SiO_2	35.45 ± 0.37	36.07 ± 0.18	34.87 ± 0.32	35.46 ± 0.35	35.89 ± 0.18	35.59 ± 0.14	35.88 ± 0.26	35.50 ± 0.17	35.21 ± 0.35	34.51 ± 0.23	33.99 ± 0.35	35.09 ± 0.30
TiO_2	2.54 ± 0.20	2.25 ± 0.11	2.30 ± 0.24	2.67 ± 0.08	1.10 ± 0.39	2.35 ± 0.29	1.32 ± 0.11	1.64 ± 0.16	1.84 ± 0.21	1.36 ± 0.44	1.85 ± 0.16	2.04 ± 0.30
Al_2O_3	19.46 ± 0.24	19.68 ± 0.18	19.10 ± 0.22	18.40 ± 0.16	19.77 ± 0.34	18.19 ± 0.16	19.54 ± 0.11	19.57 ± 0.21	19.31 ± 0.56	18.23 ± 0.20	19.13 ± 0.19	18.56 ± 0.26
FeO	18.94 ± 0.30	18.49 ± 0.28	18.97 ± 0.37	22.84 ± 0.23	20.99 ± 0.29	21.40 ± 0.31	20.78 ± 0.29	20.77 ± 0.48	21.97 ± 0.73	26.04 ± 0.43	23.33 ± 0.30	22.77 ± 0.33
MnO	0.16 ± 0.04	0.16 ± 0.03	0.16 ± 0.03	0.32 ± 0.04	0.06 ± 0.03	0.35 ± 0.04	0.03 ± 0.03	0.07 ± 0.03	0.09 ± 0.03	0.65 ± 0.05	0.08 ± 0.05	0.15 ± 0.05
MgO	9.82 ± 0.34	10.30 ± 0.08	10.10 ± 0.21	7.58 ± 0.13	9.12 ± 0.15	8.61 ± 0.22	9.47 ± 0.15	9.04 ± 0.21	8.04 ± 0.27	5.89 ± 0.14	7.07 ± 0.15	7.49 ± 0.20
CaO	0.01 ± 0.01	0.01 ± 0.01	0.00 ± 0.00	0.02 ± 0.02	0.03 ± 0.03	0.01 ± 0.01	0.00 ± 0.01	0.02 ± 0.01	0.01 ± 0.01	0.01 ± 0.01	0.00 ± 0.00	0.05 ± 0.06
Na_2O	0.66 ± 0.09	0.25 ± 0.03	0.21 ± 0.04	0.11 ± 0.03	0.17 ± 0.04	0.30 ± 0.06	0.23 ± 0.03	0.83 ± 0.08	0.73 ± 0.13	0.06 ± 0.01	0.18 ± 0.04	0.53 ± 0.11
K_2O	9.43 ± 0.23	9.67 ± 0.09	9.60 ± 0.18	9.68 ± 0.12	9.50 ± 0.17	9.62 ± 0.11	9.15 ± 0.12	9.08 ± 0.11	9.30 ± 0.15	9.98 ± 0.13	9.62 ± 0.24	9.57 ± 0.12
F	0.23 ± 0.02	0.22 ± 0.02	0.22 ± 0.03	0.22 ± 0.02	0.21 ± 0.03	0.37 ± 0.03	0.49 ± 0.03	0.51 ± 0.03	0.59 ± 0.04	0.49 ± 0.04	0.45 ± 0.03	0.45 ± 0.04
Total	96.70 ± 0.38	97.10 ± 0.21	95.55 ± 0.39	97.30 ± 0.36	96.86 ± 0.41	96.80 ± 0.38	96.89 ± 0.35	97.03 ± 0.37	97.09 ± 0.30	97.21 ± 0.28	95.70 ± 0.44	96.69 ± 0.36
Si	2.66	2.69	2.66	2.70	2.71	2.71	2.71	2.68	2.68	2.70	2.65	2.70
Ti	0.14	0.13	0.13	0.15	0.06	0.13	0.08	0.09	0.11	0.08	0.11	0.12
Al	1.72	1.73	1.72	1.65	1.76	1.63	1.74	1.74	1.73	1.68	1.76	1.68
Fe	1.19	1.15	1.21	1.45	1.32	1.36	1.31	1.31	1.40	1.70	1.52	1.46
Mn	0.01	0.01	0.01	0.02	0.00	0.02	0.00	0.00	0.01	0.04	0.01	0.01
Mg	1.10	1.14	1.15	0.86	1.03	0.98	1.06	1.02	0.91	0.69	0.82	0.86
Ca	0.00	0.00	0.00	0.00	0.00	0.00	0.00	0.00	0.00	0.00	0.00	0.00
Na	0.10	0.04	0.03	0.02	0.03	0.04	0.03	0.12	0.11	0.01	0.03	0.08
K	0.90	0.92	0.93	0.94	0.91	0.94	0.88	0.88	0.90	0.99	0.96	0.94
F	0.05	0.05	0.05	0.05	0.05	0.09	0.12	0.12	0.14	0.12	0.11	0.11
Sum	7.83	7.80	7.84	7.80	7.82	7.83	7.81	7.85	7.85	7.89	7.85	7.85
n	15	17	15	19	14	18	17	17	14	15	14	18

Tab. A5 Muscovite rim compositions (11 O basis).

Sample	16	33	39	40	48	49	50	52	54	55	56	57
SiO_2	45.22 ± 0.51	46.09 ± 0.34	45.45 ± 0.38	44.69 ± 0.13	45.77 ± 0.12	45.15 ± 0.35	45.32 ± 0.17	45.77 ± 0.14	45.50 ± 0.31	45.64 ± 0.23	45.29 ± 0.18	45.41 ± 0.16
TiO_2	0.65 ± 0.09	0.31 ± 0.03	0.45 ± 0.04	0.27 ± 0.03	0.74 ± 0.14	1.53 ± 0.15	0.91 ± 0.04	0.58 ± 0.20	1.30 ± 0.71	0.54 ± 0.03	0.76 ± 0.11	0.73 ± 0.17
Al_2O_3	35.95 ± 0.33	35.41 ± 0.26	35.92 ± 0.20	36.90 ± 0.17	35.31 ± 0.20	34.41 ± 0.64	35.15 ± 0.25	34.87 ± 0.29	35.17 ± 0.53	35.25 ± 0.23	35.34 ± 0.30	36.06 ± 0.25
FeO	1.27 ± 0.10	1.89 ± 0.13	0.90 ± 0.08	0.81 ± 0.05	1.31 ± 0.11	1.38 ± 0.11	1.50 ± 0.10	1.64 ± 0.16	1.21 ± 0.11	1.50 ± 0.09	1.35 ± 0.13	1.19 ± 0.07
MnO	0.01 ± 0.01	0.02 ± 0.02	0.01 ± 0.02	0.01 ± 0.01	0.03 ± 0.02	0.01 ± 0.02	0.05 ± 0.03	0.02 ± 0.02	0.01 ± 0.01	0.02 ± 0.02	0.03 ± 0.02	0.01 ± 0.01
MgO	0.58 ± 0.07	0.65 ± 0.07	0.68 ± 0.05	0.41 ± 0.04	0.72 ± 0.07	0.81 ± 0.13	0.65 ± 0.05	0.73 ± 0.07	0.69 ± 0.11	0.84 ± 0.04	0.68 ± 0.06	0.54 ± 0.03
CaO	0.01 ± 0.01	0.01 ± 0.01	0.01 ± 0.01	0.01 ± 0.01	0.01 ± 0.01	0.01 ± 0.01	0.00 ± 0.01	0.01 ± 0.01	0.01 ± 0.01	0.01 ± 0.01	0.01 ± 0.01	0.00 ± 0.01
Na_2O	0.98 ± 0.06	1.48 ± 0.18	1.92 ± 0.15	2.06 ± 0.06	0.74 ± 0.04	0.77 ± 0.06	0.96 ± 0.03	0.45 ± 0.04	0.77 ± 0.05	0.74 ± 0.03	0.68 ± 0.02	1.09 ± 0.04
K_2O	10.34 ± 0.09	9.49 ± 0.24	8.84 ± 0.30	8.40 ± 0.11	10.88 ± 0.08	10.56 ± 0.08	10.47 ± 0.07	11.36 ± 0.10	10.64 ± 0.08	10.66 ± 0.06	10.96 ± 0.07	10.11 ± 0.07
F	0.15 ± 0.03	0.05 ± 0.03	0.06 ± 0.02	0.03 ± 0.02	0.06 ± 0.02	0.09 ± 0.03	0.09 ± 0.03	0.24 ± 0.03	0.03 ± 0.02	0.06 ± 0.03	0.04 ± 0.02	0.04 ± 0.02
Total	95.15 ± 0.79	95.39 ± 0.49	94.24 ± 0.65	93.60 ± 0.19	95.59 ± 0.24	94.73 ± 0.22	95.12 ± 0.39	95.67 ± 0.17	95.32 ± 0.28	95.26 ± 0.43	95.15 ± 0.29	95.18 ± 0.19
Si	3.02	3.07	3.04	3.00	3.05	3.04	3.04	3.07	3.04	3.05	3.04	3.03
Ti	0.03	0.02	0.02	0.01	0.04	0.08	0.05	0.03	0.07	0.03	0.04	0.04
Al	2.83	2.78	2.83	2.92	2.78	2.73	2.78	2.75	2.77	2.78	2.79	2.83
Fe	0.07	0.10	0.05	0.05	0.07	0.08	0.08	0.09	0.07	0.08	0.08	0.07
Mn	0.00	0.00	0.00	0.00	0.00	0.00	0.00	0.00	0.00	0.00	0.00	0.00
Mg	0.06	0.06	0.07	0.04	0.07	0.08	0.06	0.07	0.07	0.08	0.07	0.05
Ca	0.00	0.00	0.00	0.00	0.00	0.00	0.00	0.00	0.00	0.00	0.00	0.00
Na	0.13	0.19	0.25	0.27	0.10	0.10	0.12	0.06	0.10	0.10	0.09	0.14
K	0.88	0.81	0.75	0.72	0.93	0.91	0.90	0.97	0.91	0.91	0.94	0.86
F	0.03	0.01	0.01	0.01	0.01	0.02	0.02	0.05	0.01	0.01	0.01	0.01
Sum	7.03	7.03	7.02	7.02	7.03	7.02	7.04	7.04	7.01	7.03	7.04	7.02
n	15	16	11	15	16	16	16	14	14	15	15	15

Sample	59	60	62	63	65	66	73	76	81	82	84	85
SiO_2	45.16 ± 0.56	45.48 ± 0.15	45.52 ± 0.24	45.58 ± 0.46	45.06 ± 0.15	45.80 ± 0.23	45.41 ± 0.46	45.24 ± 0.29	44.92 ± 0.36	45.82 ± 0.16	45.89 ± 0.13	45.57 ± 0.14
TiO_2	0.77 ± 0.09	0.77 ± 0.03	0.97 ± 0.14	0.72 ± 0.07	0.19 ± 0.04	0.80 ± 0.06	0.64 ± 0.06	0.67 ± 0.07	0.63 ± 0.07	0.45 ± 0.06	0.67 ± 0.03	0.74 ± 0.05
Al_2O_3	35.32 ± 0.23	34.91 ± 0.23	35.36 ± 0.24	34.73 ± 0.25	36.39 ± 0.23	33.28 ± 0.34	35.70 ± 0.27	35.18 ± 0.14	34.94 ± 0.27	34.47 ± 0.33	34.84 ± 0.19	34.09 ± 0.18
FeO	1.59 ± 0.09	1.38 ± 0.07	1.22 ± 0.08	1.73 ± 0.06	1.32 ± 0.05	2.33 ± 0.12	1.17 ± 0.07	1.26 ± 0.06	2.13 ± 0.08	2.17 ± 0.10	1.70 ± 0.07	2.02 ± 0.07
MnO	0.04 ± 0.02	0.02 ± 0.02	0.03 ± 0.03	0.04 ± 0.03	0.01 ± 0.01	0.05 ± 0.02	0.02 ± 0.02	0.01 ± 0.01	0.01 ± 0.01	0.04 ± 0.03	0.02 ± 0.02	0.02 ± 0.02
MgO	0.63 ± 0.04	0.93 ± 0.07	0.65 ± 0.04	0.86 ± 0.06	0.54 ± 0.06	0.99 ± 0.07	0.70 ± 0.06	0.76 ± 0.09	0.64 ± 0.06	0.78 ± 0.07	0.68 ± 0.03	0.85 ± 0.07
CaO	0.01 ± 0.01	0.00 ± 0.00	0.01 ± 0.01	0.01 ± 0.01	0.01 ± 0.01	0.00 ± 0.00	0.01 ± 0.01	0.01 ± 0.01	0.01 ± 0.01	0.00 ± 0.01	0.02 ± 0.02	0.01 ± 0.01
Na_2O	0.88 ± 0.03	0.88 ± 0.04	1.27 ± 0.05	0.58 ± 0.04	1.23 ± 0.07	0.67 ± 0.04	1.23 ± 0.04	1.06 ± 0.05	1.05 ± 0.04	0.48 ± 0.03	0.78 ± 0.03	0.66 ± 0.02
K_2O	10.43 ± 0.06	10.40 ± 0.08	10.08 ± 0.08	10.92 ± 0.14	9.85 ± 0.09	10.96 ± 0.11	9.88 ± 0.06	10.04 ± 0.10	10.14 ± 0.06	11.21 ± 0.08	10.83 ± 0.07	10.80 ± 0.08
F	0.03 ± 0.01	0.05 ± 0.02	0.03 ± 0.02	0.06 ± 0.02	0.03 ± 0.02	0.09 ± 0.02	0.11 ± 0.02	0.13 ± 0.03	0.15 ± 0.01	0.16 ± 0.02	0.12 ± 0.02	0.13 ± 0.02
Total	94.85 ± 0.76	94.83 ± 0.23	95.13 ± 0.30	95.23 ± 0.46	94.63 ± 0.17	94.99 ± 0.25	94.87 ± 0.57	94.37 ± 0.28	94.62 ± 0.46	95.58 ± 0.37	95.54 ± 0.24	94.90 ± 0.22
Si	3.03	3.05	3.04	3.06	3.02	3.10	3.04	3.05	3.03	3.08	3.07	3.07
Ti	0.04	0.04	0.05	0.04	0.01	0.04	0.03	0.03	0.03	0.02	0.03	0.04
Al	2.80	2.76	2.78	2.75	2.87	2.65	2.82	2.79	2.78	2.73	2.75	2.71
Fe	0.09	0.08	0.07	0.10	0.07	0.13	0.07	0.07	0.12	0.12	0.09	0.11
Mn	0.00	0.00	0.00	0.00	0.00	0.00	0.00	0.00	0.00	0.00	0.00	0.00
Mg	0.06	0.09	0.06	0.09	0.05	0.10	0.07	0.08	0.06	0.08	0.07	0.09
Ca	0.00	0.00	0.00	0.00	0.00	0.00	0.00	0.00	0.00	0.00	0.00	0.00
Na	0.11	0.11	0.16	0.08	0.16	0.09	0.16	0.14	0.14	0.06	0.10	0.09
K	0.89	0.89	0.86	0.93	0.84	0.94	0.84	0.86	0.87	0.96	0.92	0.93
F	0.01	0.01	0.01	0.01	0.01	0.02	0.02	0.03	0.03	0.03	0.02	0.03
Sum	7.03	7.03	7.03	7.04	7.04	7.05	7.02	7.02	7.05	7.05	7.04	7.04
n	16	15	17	15	12	17	15	15	15	15	16	15

Tab. A6 Plagioclase rim compositions (8 O basis).

Sample	16	33	39	40	48	49	50	52	54	55	56	57
SiO_2	60.86 ± 0.15	62.44 ± 0.70	64.78 ± 0.14	61.66 ± 0.27	61.42 ± 0.32	60.83 ± 0.23	65.00 ± 0.18	63.25 ± 0.32	62.54 ± 0.15	61.73 ± 0.37	62.75 ± 0.19	62.75 ± 0.29
Al_2O_3	24.51 ± 0.11	23.36 ± 0.43	22.05 ± 0.14	23.96 ± 0.14	23.94 ± 0.20	24.51 ± 0.11	21.64 ± 0.13	22.91 ± 0.23	23.28 ± 0.08	23.80 ± 0.19	23.25 ± 0.13	23.15 ± 0.18
FeO	0.22 ± 0.04	0.19 ± 0.06	0.05 ± 0.04	0.30 ± 0.10	0.34 ± 0.14	0.14 ± 0.09	0.35 ± 0.09	0.32 ± 0.08	0.18 ± 0.11	0.13 ± 0.06	0.21 ± 0.05	0.20 ± 0.08
MgO	0.00 ± 0.01	0.01 ± 0.01	0.01 ± 0.01	0.01 ± 0.01	0.00 ± 0.01	0.00 ± 0.00	0.01 ± 0.01	0.01 ± 0.02	0.01 ± 0.01	0.01 ± 0.01	0.00 ± 0.01	0.01 ± 0.01
CaO	5.98 ± 0.07	4.74 ± 0.48	3.01 ± 0.11	5.38 ± 0.18	5.59 ± 0.13	5.97 ± 0.15	2.62 ± 0.11	4.28 ± 0.08	4.60 ± 0.06	5.26 ± 0.25	4.69 ± 0.13	4.46 ± 0.19
Na_2O	8.32 ± 0.08	9.16 ± 0.31	10.18 ± 0.09	8.82 ± 0.16	8.44 ± 0.12	8.38 ± 0.08	10.30 ± 0.09	9.22 ± 0.13	9.14 ± 0.11	8.74 ± 0.17	8.98 ± 0.12	9.32 ± 0.13
K_2O	0.13 ± 0.02	0.09 ± 0.02	0.07 ± 0.02	0.06 ± 0.01	0.11 ± 0.06	0.13 ± 0.05	0.08 ± 0.01	0.20 ± 0.10	0.11 ± 0.03	0.11 ± 0.04	0.14 ± 0.04	0.07 ± 0.02
Total	100.04 ± 0.29	99.97 ± 0.33	100.15 ± 0.25	100.18 ± 0.35	99.83 ± 0.65	99.95 ± 0.25	99.99 ± 0.32	100.18 ± 0.47	99.86 ± 0.21	99.78 ± 0.28	100.03 ± 0.27	99.96 ± 0.32
Si	2.71	2.77	2.85	2.74	2.73	2.71	2.87	2.80	2.78	2.75	2.78	2.78
Al	1.29	1.22	1.14	1.25	1.26	1.29	1.12	1.19	1.22	1.25	1.21	1.21
Fe	0.01	0.01	0.00	0.01	0.01	0.01	0.01	0.01	0.01	0.00	0.01	0.01
Mg	0.00	0.00	0.00	0.00	0.00	0.00	0.00	0.00	0.00	0.00	0.00	0.00
Ca	0.29	0.23	0.14	0.26	0.27	0.28	0.12	0.20	0.22	0.25	0.22	0.21
Na	0.72	0.79	0.87	0.76	0.73	0.72	0.88	0.79	0.79	0.75	0.77	0.80
K	0.01	0.00	0.00	0.00	0.01	0.01	0.00	0.01	0.01	0.01	0.01	0.00
Sum	5.01	5.02	5.01	5.02	5.00	5.01	5.01	5.01	5.01	5.01	5.00	5.02
n	19	18	15	14	19	18	18	16	16	15	19	18

Sample	59	60	62	63	65	66	73	76	81	82	84	85
SiO_2	63.20 ± 0.13	63.33 ± 0.24	63.06 ± 0.28	62.05 ± 0.22	65.91 ± 1.48	62.96 ± 0.33	60.25 ± 0.14	58.47 ± 0.58	59.42 ± 0.31	63.04 ± 1.25	58.04 ± 0.30	58.51 ± 0.33
Al_2O_3	22.90 ± 0.12	22.73 ± 0.11	22.99 ± 0.16	23.86 ± 0.14	20.84 ± 0.35	23.07 ± 0.20	25.06 ± 0.14	25.75 ± 0.38	25.27 ± 0.15	23.18 ± 0.70	25.86 ± 0.19	25.90 ± 0.18
FeO	0.22 ± 0.09	0.13 ± 0.08	0.29 ± 0.08	0.25 ± 0.07	0.31 ± 0.12	0.10 ± 0.06	0.08 ± 0.03	0.11 ± 0.06	0.11 ± 0.08	0.18 ± 0.07	0.24 ± 0.04	0.13 ± 0.10
MgO	0.01 ± 0.01	0.01 ± 0.01	0.01 ± 0.01	0.00 ± 0.01	0.00 ± 0.00	0.00 ± 0.01	0.00 ± 0.01	0.01 ± 0.01	0.00 ± 0.00	0.00 ± 0.00	0.01 ± 0.01	0.01 ± 0.01
CaO	4.10 ± 0.10	3.82 ± 0.10	4.41 ± 0.09	5.17 ± 0.14	1.62 ± 0.21	4.39 ± 0.25	6.60 ± 0.11	7.78 ± 0.36	7.07 ± 0.13	4.59 ± 0.32	8.17 ± 0.17	7.83 ± 0.18
Na_2O	9.54 ± 0.10	9.68 ± 0.13	9.25 ± 0.10	8.88 ± 0.15	10.88 ± 0.25	9.29 ± 0.21	8.06 ± 0.07	7.32 ± 0.24	7.69 ± 0.13	9.04 ± 0.27	7.05 ± 0.11	7.29 ± 0.09
K_2O	0.09 ± 0.02	0.07 ± 0.02	0.06 ± 0.02	0.11 ± 0.02	0.09 ± 0.04	0.13 ± 0.02	0.08 ± 0.02	0.09 ± 0.02	0.10 ± 0.02	0.21 ± 0.04	0.11 ± 0.03	0.15 ± 0.11
Total	100.06 ± 0.27	99.76 ± 0.35	100.06 ± 0.53	100.34 ± 0.18	99.65 ± 1.89	99.94 ± 0.26	100.13 ± 0.21	99.52 ± 0.74	99.65 ± 0.40	100.25 ± 0.27	99.47 ± 0.29	99.81 ± 0.30
Si	2.80	2.81	2.79	2.75	2.91	2.79	2.68	2.63	2.66	2.79	2.61	2.62
Al	1.19	1.19	1.20	1.24	1.08	1.20	1.31	1.36	1.33	1.21	1.37	1.37
Fe	0.01	0.00	0.01	0.01	0.01	0.00	0.00	0.00	0.00	0.01	0.01	0.00
Mg	0.00	0.00	0.00	0.00	0.00	0.00	0.00	0.00	0.00	0.00	0.00	0.00
Ca	0.19	0.18	0.21	0.25	0.08	0.21	0.31	0.37	0.34	0.22	0.39	0.38
Na	0.82	0.83	0.79	0.76	0.93	0.80	0.70	0.64	0.67	0.77	0.62	0.63
K	0.01	0.00	0.00	0.01	0.01	0.01	0.00	0.00	0.01	0.01	0.01	0.01
Sum	5.02	5.02	5.01	5.02	5.02	5.01	5.01	5.01	5.01	5.00	5.01	5.01
n	17	20	16	19	13	14	18	19	18	15	17	16